

Title	アナターゼ構造のチタン酸化物に生じる不純物や欠陥の生成安定性に関する計算科学的解析
Author(s)	ABHISHEK, RAGHAV
Citation	
Issue Date	2022-09
Type	Thesis or Dissertation
Text version	ETD
URL	<a href="http://hdl.handle.net/10119/18135">http://hdl.handle.net/10119/18135</a>
Rights	
Description	Supervisor:前園 涼, 先端科学技術研究科, 博士

***Ab initio* analysis of the formation stability of defects and dopant analysis in titanium dioxide with anatase structure**

Abhishek Raghav

Japan Advanced Institute of Science and Technology

# Doctoral Dissertation

*Ab initio* analysis of the formation stability of defects and dopant  
analysis in titanium dioxide with anatase structure

Abhishek Raghav

Supervisor: Ryo Maezono

Graduate School of Advanced Science and Technology  
Japan Advanced Institute of Science and Technology  
Information Science  
September, 2022

# Abstract

TiO<sub>2</sub> (anatase polymorph) is a wide band gap semiconductor, studied for its interesting optoelectronic properties. Intrinsic (or native) defects and extrinsic defects (dopants) can alter the band structure of TiO<sub>2</sub> in interesting ways, which can render this material suitable for certain optoelectronic applications like photocatalysts and transparent conducting oxides.

In this work, we perform a comprehensive *ab initio* electronic structure analysis of undoped and doped anatase systems using density functional theory aided by the Hubbard correction (DFT+*U*). Such an analysis could help in selecting better dopants for transparent conducting oxide (TCO) and photocatalytic applications. To avoid fitting *U* parameter to properties like band gap, we use the linear response *ansatz* to systematically compute *U* for the dopant atoms. The dopants considered are Nb, Ta, Mo, V, W, Cr, Co, Cu, La and Ce. Electronic structures of anatase with intrinsic defects are also reported. The intrinsic point defects considered are oxygen vacancies (*V<sub>O</sub>*), oxygen interstitials (*O<sub>i</sub>*), titanium vacancies (*V<sub>Ti</sub>*) and titanium interstitials (*Ti<sub>i</sub>*).

Out of all the intrinsic defects considered, *V<sub>Ti</sub>* and *Ti<sub>i</sub>* were found to be the most stable under equilibrium condition. *V<sub>O</sub>* and *Ti<sub>i</sub>* were found to form localized states in the band gap. In case of *V<sub>O</sub>*, the localized states were formed close to the conduction band. *Ti<sub>i</sub>* also formed mid gap defect states. Electron transition from the defect states to the conduction band could impart intrinsic *n*-type conductivity to anatase.

In the case of the dopant atoms considered, dopants like Nb, Ta, V and Ce formed states in the conduction band with no mid gap states. Dopants Nb, Ta and W were found to have the Fermi levels positioned near the conduction band edge, indicating these systems to exhibit *n*-type conductivity. Other dopants like Mo, W, Cr, Co, Cu formed states in the band-gap. Mid gap states could be undesirable for TCO applications because the electron transitions to/from the mid gap states would reduce the transparency. Dopants which form states close to the conduction or the valence band affect the curvature of these bands. Effective masses of charge carriers are defined by band curvatures and hence are altered when dopants perturb the band structure. Effective mass of electrons at the conduction band edge was found to be higher in doped systems than in pristine TiO<sub>2</sub>. Dopants also reduced the parabolicity of bands in general which leads to differences in effective mass values computed using different algebraic definitions.

This study provides an insight into how native defects and dopants affect the electronic structure of the host anatase material by forming impurity states and/or altering the band curvature, which in turn affects the optoelectronic properties of the material. Based on electronic structure and effective mass analysis, Nb, Ta and W are identified to exhibit higher transparency and conductivity as compared to the other dopants considered here. The theoretical results presented here, increase our understanding and show the potential of dopants to alter the properties in anatase TiO<sub>2</sub>.

Keywords: *VASP*, *ab initio*, *TiO<sub>2</sub>*, *transparent conducting oxide*, *effective mass*, *formation energy*

# Acknowledgements

This research work would not have been possible without the guidance and support of a number of people. First of all, I would like to thank my research supervisor Prof. Ryo Maezono for his guidance, constant support and help throughout my research journey. His guidance during thesis documentation, manuscript preparation and preparation of presentations was very useful. I would also like to thank Assoc. Prof. Emila Panda from IIT Gandhinagar (India), who was a collaborator, for her guidance and help in preparing the manuscripts. I also acknowledge the help and guidance from Assoc. Prof. Shogo Okada (second supervisor), Assoc. Prof. Kenta Hongo (minor research supervisor) and Dr. Kousuke Nakano. I would also like to thank the thesis committee members; Prof. Yoshifumi Oshima, Prof. Satoshi Tojo, Assoc. Prof. Kenta Hongo and Prof. Tamio Oguchi for taking time to check my dissertation and presentation and provide valuable feedback. The computations in this research were performed using supercomputers at JAIST and I would like to thank RCACI at JAIST for providing access and help during times of difficulties. I got a lot of support from our lab staff; Kida-san, Kitagawa-san and Fujita-san, who helped me a lot in keeping up with the deadlines. I would like to thank my lab mates (Genki-san, Okumura-san, Adie-san, Song-san, Abdul-san and Rohit-san) for their constant support, help and encouragement. Finally (and very important), I would like to thank my parents and family members for their support and encouragement during difficult times.

Thank you very much.

# Contents

<b>Abstract</b>	<b>i</b>
List of Figures . . . . .	vi
List of Tables . . . . .	vii
<b>1 Introduction</b>	<b>1</b>
1.1 Background . . . . .	1
1.2 Motivation . . . . .	2
1.3 Problem Statements . . . . .	4
1.4 Outline . . . . .	4
<b>2 Methodology</b>	<b>5</b>
2.1 The many-body Schrödinger equation . . . . .	5
2.2 From wave functions to electron density . . . . .	7
2.3 The Hohenberg-Kohn theorems . . . . .	7
2.4 Kohn-Sham equations . . . . .	8
2.5 Basis set expansion and energy cutoffs . . . . .	8
2.6 $K$ points and Brillouin zone integrals . . . . .	10
2.7 Smearing . . . . .	12
2.8 Pseudopotentials . . . . .	13
2.9 Exchange-correlation (XC) functionals . . . . .	13
2.10 Hubbard $U$ correction (DFT+ $U$ ) . . . . .	16
2.10.1 Determining the Hubbard $U$ parameter using the linear response approach	16
2.11 Formation energy of point defects . . . . .	17
2.12 Force calculation and geometry optimization . . . . .	18
2.13 Effective masses of charge carriers . . . . .	18
2.13.1 Curvature effective mass . . . . .	19
2.13.2 Transport effective mass . . . . .	20
2.13.3 Kane quasi-linear dispersion . . . . .	20
2.13.4 Optical effective mass . . . . .	21
<b>3 Pristine Anatase</b>	<b>22</b>
3.1 Lattice and electronic structure . . . . .	23
<b>4 Intrinsic Defects</b>	<b>25</b>
4.1 Geometrical distortion due to native defects . . . . .	25
4.2 Neutral and charged oxygen vacancies ( $V_O$ , $V_O^{+1}$ , $V_O^{+2}$ ) . . . . .	26
4.3 Neutral and charged titanium interstitials ( $Ti_i$ , $Ti_i^{+1}$ , $Ti_i^{+2}$ , $Ti_i^{+3}$ , $Ti_i^{+4}$ ) . . . . .	28
4.4 Titanium vacancies ( $V_{Ti}$ ) and oxygen interstitials ( $O_i$ ) . . . . .	30
4.5 Stability of native defects: Formation energy analysis . . . . .	31

<b>5</b>	<b>Dopants</b>	<b>33</b>
5.1	Niobium ( $Nb_{Ti}$ ) . . . . .	33
5.2	Tantalum ( $Ta_{Ti}$ ) . . . . .	34
5.3	Vanadium ( $V_{Ti}$ ) . . . . .	36
5.4	Molybdenum ( $Mo_{Ti}$ ) . . . . .	38
5.5	Tungsten ( $W_{Ti}$ ) . . . . .	40
5.6	Chromium ( $Cr_{Ti}$ ) . . . . .	42
5.7	Lanthanum ( $La_{Ti}$ ) . . . . .	44
5.8	Copper ( $Cu_{Ti}$ ) . . . . .	46
5.9	Cobalt ( $Co_{Ti}$ ) . . . . .	47
5.10	Cerium ( $Ce_{Ti}$ ) . . . . .	50
5.11	Effective mass analysis . . . . .	51
	5.11.1 Pristine anatase . . . . .	51
	5.11.2 Dopants . . . . .	52
<b>6</b>	<b>Conclusion</b>	<b>56</b>

# List of Figures

1.1	Possible cases of defect state position for doped anatase. a) The defect state acts as a shallow donor, b) localized mid-gap state formed in the gap and c) acceptor-like state . . . . .	3
2.1	Workflow for a self-consistent solution of Kohn-Sham equations . . . . .	9
2.2	Convergence test for cutoff energy for anatase . . . . .	11
2.3	Convergence test for $k$ spacing for anatase . . . . .	12
2.4	Jacob's ladder of DFT functionals (adapted from Sholl <i>et al.</i> [1]) . . . . .	15
2.5	Linear fitting of $d$ orbital occupation for the Ti site in $\text{TiO}_2$ . . . . .	17
2.6	Curvature, transport and optical effective mass . . . . .	21
3.1	Schematic of (a) anatase supercell, (b) the first brillouin zone of anatase lattice with high symmetry k points and (c) distorted $\text{TiO}_6$ octahedron of anatase. The two vertical Ti-O (apical) bonds are slightly longer than the other four equatorial Ti-O bonds. . . . .	22
3.2	Band structure (a) and PDOS (b) of anatase. Points $P_1$ and $P_2$ correspond to the CBM and VBM respectively and $E_g$ is the indirect band gap (2.44 eV). Fermi energy ( $E_F$ ) has been shifted to 0 eV. . . . .	24
4.1	A conventional cell of anatase showing the direction of forces acting on the neighbouring atoms to the defect site (called as the defect associated atoms). The defect site has been marked as X. The figures depict anatase with (a) $V_O$ , (b) $Ti_i$ , (c) $V_{Ti}$ and (d) $O_i$ respectively. . . . .	25
4.2	DOS of pure anatase (a) and anatase with $V_O$ , $V_O^{+1}$ and $V_O^{+2}$ (b)-(d) respectively with Ti $3d$ states also shown. Black dotted line represents the $E_F$ and VBM of pure anatase has been chosen as the reference for all the plots. . . . .	27
4.3	DOS of pure anatase (a) and anatase with $Ti_i$ , $Ti_i^{+1}$ , $Ti_i^{+2}$ , $Ti_i^{+3}$ and $Ti_i^{+4}$ (b)-(f) respectively with Ti $3d$ states also shown. Black dotted line represents the $E_F$ and VBM of pure anatase has been chosen as the reference for all the plots. . . . .	29
4.4	Total DOS (a) and PDOS (b) of anatase. DOS of anatase with $V_{Ti}$ (c) and $O_i$ (d). Red dotted line in (c) and (d) represents O $2p$ states (scaled by 5 times) due to the defect associated atoms. Black dotted line represents the $E_F$ and VBM of pure anatase has been chosen as the reference for all the plots. . . . .	30
4.5	Defect formation energies of native defects as a function of Fermi level ( $E_F$ ) in O-poor (a) and O-rich (b) conditions. The lower and upper limits of fermi level correspond to VBM and CBM respectively. . . . .	31
5.1	PDOS of Nb-doped anatase. $E_F$ has been shifted to 0 eV . . . . .	33
5.2	Band structure of Nb-doped anatase. $E_F$ has been shifted to 0 eV . . . . .	34
5.3	PDOS of Ta-doped anatase. $E_F$ has been shifted to 0 eV . . . . .	35



5.4	Band structure of Ta-doped anatase. $E_F$ has been shifted to 0 eV . . . . .	36
5.5	PDOS of V-doped anatase. $E_F$ has been shifted to 0 eV . . . . .	37
5.6	Band structure of V-doped anatase. $E_F$ has been shifted to 0 eV . . . . .	37
5.7	PDOS of Mo-doped anatase. $E_F$ has been shifted to 0 eV . . . . .	38
5.8	Band structure of Mo-doped anatase. $E_F$ has been shifted to 0 eV . . . . .	39
5.9	Charge density isosurface for Mo-doped anatase plotted in the region of mid-gap state . . . . .	39
5.10	PDOS of W-doped anatase. $E_F$ has been shifted to 0 eV . . . . .	40
5.11	Band structure of W-doped anatase. $E_F$ has been shifted to 0 eV . . . . .	41
5.12	Charge density isosurface for W-doped anatase plotted on a 2d surface (containing W dopant atom) in the region of mid-gap state . . . . .	41
5.13	PDOS of Cr-doped anatase. $E_F$ has been shifted to 0 eV . . . . .	42
5.14	Band structure of Cr-doped anatase. $E_F$ has been shifted to 0 eV . . . . .	43
5.15	Charge density isosurface for Cr-doped anatase plotted on a horizontal layer (containing Cr dopant atom) in the region of mid-gap state . . . . .	43
5.16	PDOS of La-doped anatase. $E_F$ has been shifted to 0 eV . . . . .	44
5.17	Band structure of La-doped anatase. $E_F$ has been shifted to 0 eV . . . . .	45
5.18	Charge density isosurface for La-doped anatase plotted in the region of localized states formed near the valence band edge . . . . .	45
5.19	PDOS of Cu-doped anatase. $E_F$ has been shifted to 0 eV . . . . .	46
5.20	Band structure of Cu-doped anatase. $E_F$ has been shifted to 0 eV . . . . .	47
5.21	Charge density isosurface for Cu-doped anatase plotted in the region of localized states formed near the valence band edge (a) and near the conduction band edge (b) . . . . .	47
5.22	PDOS of Co-doped anatase. $E_F$ has been shifted to 0 eV . . . . .	48
5.23	Band structure of Co-doped anatase. $E_F$ has been shifted to 0 eV . . . . .	49
5.24	Charge density isosurface for a horizontal layer containing Co atom plotted in the region of localized states formed near the valence band edge (a) and near the conduction band edge (b) . . . . .	49
5.25	PDOS of Ce-doped anatase. $E_F$ has been shifted to 0 eV . . . . .	50
5.26	Band structure of Ce-doped anatase. $E_F$ has been shifted to 0 eV . . . . .	51
5.27	Band dispersion fitting at the conduction band edge (a) and valence band edge (b), along $\Gamma - X$ direction . . . . .	52
5.28	(a) Computed effective masses (as multiples of electron rest mass) of electrons for various doped systems and (b) corresponding $\alpha$ values . . . . .	53
5.29	Band dispersion fitting at the conduction band edge along $\Gamma - X$ direction for (a) Nb-doped anatase and (b) Ta-doped anatase . . . . .	54
5.30	(a) Effective masses computed for electrons in the mid-gap states and (b) corresponding $\alpha$ values . . . . .	55
5.31	(a) Computed effective masses (as multiples of electron rest mass) of holes for various doped systems, (b) Band dispersion fitting at the valence band edge along $\Gamma - X$ direction for Co-doped anatase . . . . .	55

# List of Tables

2.1	Valence configurations of various elements utilized in the current work . . . . .	14
2.2	$U_{eff}$ values of various elements computed using Linear response method . . . . .	17
3.1	Lattice parameters, bond lengths (in Å), band gap (in eV) and Bader charges for anatase. . . . .	24
4.1	Distances (Å) of the defect associated atoms from the defect site . . . . .	26
4.2	Charge transition levels (in eV) of various native defects with respect to the VBM	32
5.1	Change in lattice parameters and bond lengths of Nb-doped anatase with respect to pristine anatase. $\Delta_{bond}$ is the change in Nb-O bond length w.r.t. Ti-O bond length. . . . .	34
5.2	Change in lattice parameters and bond lengths of Ta-doped anatase with respect to pristine anatase. $\Delta_{bond}$ is the change in Ta-O bond length w.r.t. Ti-O bond length. . . . .	35
5.3	Change in lattice parameters and bond lengths of V-doped anatase with respect to pristine anatase. $\Delta_{bond}$ is the change in V-O bond length w.r.t. Ti-O bond length.	36
5.4	Change in lattice parameters and bond lengths of Mo-doped anatase with respect to pristine anatase . . . . .	38
5.5	Change in lattice parameters and bond lengths of W-doped anatase with respect to pristine anatase . . . . .	40
5.6	Change in lattice parameters and bond lengths of Cr-doped anatase with respect to pristine anatase . . . . .	42
5.7	Change in lattice parameters and bond lengths of La-doped anatase with respect to pristine anatase . . . . .	44
5.8	Change in lattice parameters and bond lengths of Cu-doped anatase with respect to pristine anatase . . . . .	46
5.9	Change in lattice parameters and bond lengths of Co-doped anatase with respect to pristine anatase. $\Delta_{bond}$ is the change in Co-O bond length w.r.t. Ti-O bond length. . . . .	48
5.10	Change in lattice parameters and bond lengths of Ce-doped anatase with respect to pristine anatase. $\Delta_{bond}$ is the relative change in the Ce-O bond length w.r.t Ti-O bond length . . . . .	50
5.11	Charge carrier effective masses (along $\Gamma - X$ direction) in pristine anatase . . . . .	52

# Chapter 1

## Introduction

### 1.1 Background

Electronic structure calculations are essential tools for searching new materials with desired properties, predicting properties of materials and better understanding of experimental results. Due to the availability of both massively parallel computing facilities and highly parallelized electronic structure codes, these are becoming a de facto standard to support experimental results and to understand the underlying chemistry. Material simulations are also being used for high throughput screening of materials. This has led to the development of several electronic structure codes using sophisticated techniques to take advantage of the fast hardware.

The primary objective of electronic structure codes is to compute the many-body wave function. However, a major problem arises for a system with large number of atoms. The many-body wave function is a  $3N$  dimensional quantity, which becomes very expensive to compute as the system size increases. Density functional theory (DFT) tries to alleviate this problem by computing electron density (3-dimensional) instead of directly calculating the many-body wave function. DFT is widely used to predict material properties and efforts to make DFT calculations faster and better at modelling the many-body effects are an area of active research. Many new and advanced schemes (like DFT+ $U$ , meta-GGA and hybrid functionals) have been devised to improve the predictions of DFT.

TiO<sub>2</sub> (anatase) is a chemically stable, non-toxic, low cost, and wide band-gap semiconductor. TiO<sub>2</sub> has two more polymorphs other than anatase: rutile and brookite. Anatase is more stable at lower temperatures, rutile becomes more stable at elevated temperatures (650 K) and brookite is the least stable phase [2]. Moreover, out of all the three thermodynamically stable phases, anatase is favoured because of its relatively higher activity and lower electron effective mass as compared to the others [3,4]. It is an attractive material for applications like transparent conducting oxides [5–7] and photocatalysts [8, 9]. Transparent conducting oxides (TCOs) are materials which are both transparent and conductive. TCOs have a wide range of applications like touchscreens, solar cells, flat-panel displays, light emitting diodes, transparent thin film transistors and semiconductor lasers [10]. The most widely used TCO is Sn-doped In<sub>2</sub>O<sub>3</sub> (ITO) due to its superior optoelectronic properties [11]. However, low concentration of Indium in the earth's upper continental crust ( $\approx 50$  ppb) [12] has pushed researchers for designing alternative TCOs. TiO<sub>2</sub> (anatase) has also been widely studied for its photocatalytic applications. A photocatalyst is a material which absorbs light to generate charge carriers. These energetic charge carriers can then be used to carry out or catalyse various chemical reactions for various application like obtaining useful materials (like hydrogen gas and hydrocarbons), removing pollutants

and bacteria from surfaces [13–15].

TiO<sub>2</sub> (anatase) has an experimental band gap of  $\approx 3.2$  eV [16] which makes it inherently transparent to visible light, and it also makes it a poor electrical conductor. Pristine anatase thus can't be used as a TCO because of the poor conductivity. Native defects like vacancies and interstitials, and impurities (dopants) can be used to tune the properties of this material. This is called as band-gap or band-structure tuning. Point defects in anatase introduce impurity states. Material scientists can then control the type, concentration and combination of defects and/or impurities to tune the band structure of anatase to achieve desired properties (or applications). For example, anatase thin films when doped with Niobium are found to have good conductivity, thus making this material suitable for TCO application [17]. Pristine anatase has a band gap that is too large for it to absorb visible light. It only absorbs light in the UV region and above. Hence, it is essential to reduce the band gap of anatase (red shift), so that it can absorb light of even lower frequencies and function as a photocatalyst. There have been several experimental and computational studies to achieve this objective using doping [18–20]. Thus, “defect engineering” and band structure/gap tuning of anatase to make it suitable for optoelectronic applications is an active area of research. Experiments can provide macroscopic information, but when information about what is happening at the atomic level is needed *ab initio* calculations become extremely important. DFT calculations can help in determining how intrinsic defects like vacancies and impurities (or dopants) affect the electronic structure (and properties) of anatase. The objective of this work is to utilize DFT to compute the electronic structure of doped and undoped TiO<sub>2</sub> systems and to carry a comprehensive investigation of how point defects affect electronic properties of anatase. This information can be very useful in making anatase a better transparent conducting oxide (TCO).

## 1.2 Motivation

Both intrinsic (like vacancies) and extrinsic (dopants) can alter the electronic structure of anatase in fundamental ways, which ultimately affects macroscopic optoelectronic properties.

Numerous first principle studies using density functional theory (DFT) have been carried out in the literature for the undoped and doped anatase, the obtained results were found to vary, which could be attributed to the use of computational methodology in DFT [21]. In this regard, Phattalung *et al.* computed the native defects in anatase using Local Density Approximation (LDA) exchange correlation functional and found none of these four defect states (i.e., oxygen vacancy ( $V_O$ ), oxygen interstitial ( $O_i$ ), titanium vacancy ( $V_{Ti}$ ) and titanium interstitial ( $Ti_i$ )) being formed in the band gap [22]. However, experimental data had earlier revealed formation of mid-gap states in these systems [23, 24], and therefore this discrepancy could be assigned to the self-interaction error of the LDA functional. Note here that, the more advanced methods like DFT+ $U$  and hybrid functionals could correctly predict the existence of mid-gap defect levels due to native defects and could also predict the band gap accurately to a certain extent. Morgan *et al.* used GGA+ $U$  in their calculations and found localized mid-gap states being formed due to the neutral oxygen vacancies and titanium interstitials in anatase [25].

Most of the published works till date have investigated the effect of (neutral) native defects on the electronic structure of anatase. In the current work, we used GGA+ $U$  approach in DFT to calculate the position and formation energies of various intrinsic (neutral as well as charged) defects for anatase. Apart from computing the electronic structure of these systems, in this study formation energy of all these native defects was calculated to understand the stability of these defects under different conditions.

For doped anatase systems, transition metals (Nb, Ta, V, Mo, W, Cr, Cu, Co) and two rare-earth elements (La and Ce) were considered as dopants in this study. J. Osorio Guillen *et al.* identified two types of behaviour for transition metal impurities in oxides; first in which the delocalized states are formed inside the conduction band thereby making the transparent material conductive and second in which a localized mid gap state could form which then could transform the magnetic properties of the host material, indicating the energy of the outer *d* electrons of the impurity atom playing a decisive role on the eventual position of this defect state [26]. The various cases that are possible for the position of defect states are depicted in Fig. 1.1

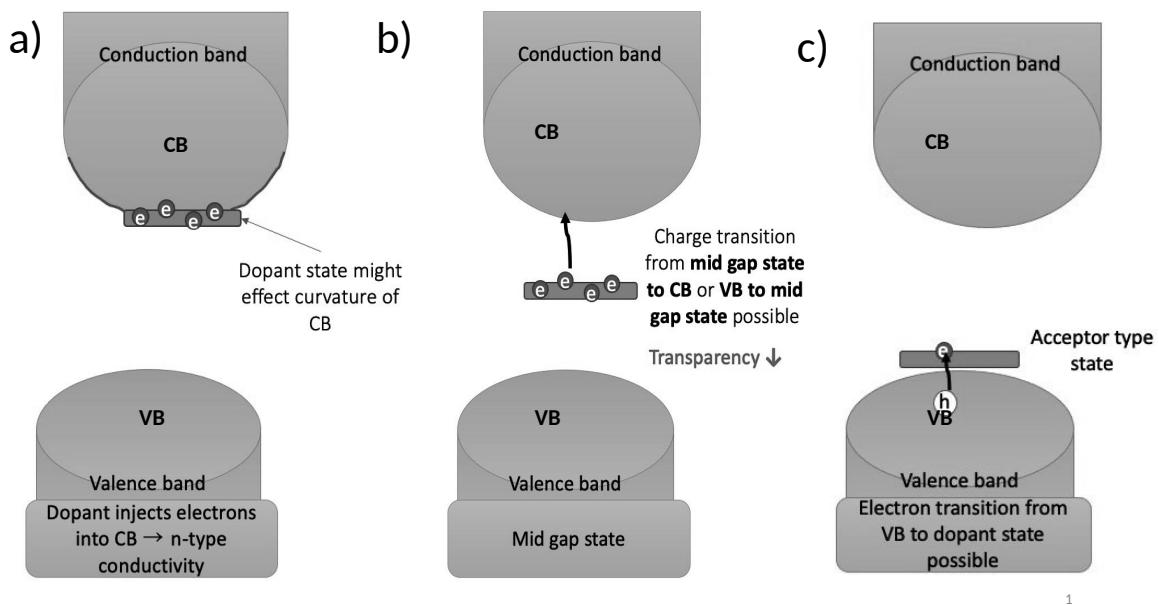


Figure 1.1: Possible cases of defect state position for doped anatase. a) The defect state acts as a shallow donor, b) localized mid-gap state formed in the gap and c) acceptor-like state

Depending upon the energy of *d* electrons, transition metal dopants might act as shallow donors, form a mid-gap state or form acceptor-like state. In the first case, the defect state is formed very close to the conduction band edge, such that the band gap is not changed much and electron transition from the defect state to conduction band can impart *n*-type conductivity to the host material. Dopants states formed near the conduction band edge might also affect the curvature of the bands, altering the effective mass of charge carriers. In the second case, a deep mid-gap state is formed. Formation of such a mid-gap state might not be good for TCO application because of the possible electron transition to and from the mid-gap state (hence reducing the transparency). In the third case, dopant forms acceptor-like state close to the valence band. This could lead to *p*-type conductivity in the host material. Again here, the dopant state might modify the band curvature, thereby modifying the effective mass of charge carriers. There are some other possibilities as well. For example, the dopant atom might form delocalized states in the conduction band, donating excess electrons in the conduction band and imparting a metallic nature to the system. Dopant atom might also form a combination of localized mid-gap and delocalized states. Thus, knowing the location of defect states and how they effect the curvature of the bands (effective mass) of the host material proves to be very important in tuning the properties of anatase using doping.

There have been several DFT studies for doped anatase systems. Earlier studies used LDA and GGA to investigate doped anatase systems [22, 27, 28]. These have obvious disadvantages of band gap underestimation and delocalization of excess electrons over the crystal due to the self interaction error. More recent studies have used the Hubbard correction (GGA+ $U$ ) [29, 30]. In almost all the studies for doped anatase using DFT+ $U$ ,  $U$  has been determined either empirically (like fitting to properties like band gap) or taken from earlier literature. We used an alternative way: computing the value of  $U$  for all the dopants consistently using the linear response approach developed by Cococcioni *et al.* [31]. Effective mass of charge carriers plays a crucial role in determining optoelectronic properties of materials. Effective mass analysis has been done for Nb-doped anatase [32], but for the other dopants, reports are quite scarce. Hence, we did a comprehensive effective mass analysis for charge carriers for the dopants considered here. We believe that this information would be crucial to both experimentalists and computational material scientists alike.

### 1.3 Problem Statements

In this work, the following research questions have been addressed:

- How do native defects affect the electronic structure of anatase? Can native defects impart intrinsic  $n$ -type conductivity?
- Which dopants might make anatase more suitable for TCO application?
- How do dopants affect the effective masses of charge carriers? Comparison of effective masses in conduction band, valence band and mid-bands (or mid gap).

### 1.4 Outline

This work is divided into 6 chapters.

- Chapter 1: Provides the background of this research. It also discusses the motivation, importance and the scope of this research. Primary objectives and existing literature are also discussed.
- Chapter 2: Methodology enumerates the existing literature concerning the methodologies used in this work, mainly that of the DFT and effective mass methods. Core principles are described, as well as unique considerations taken within this work (as well as the reasoning involved).
- Chapter 3: Results and discussion for pristine anatase.
- Chapter 4: Results and discussion for anatase with intrinsic defects.
- Chapter 5: Results and discussion for doped anatase systems.
- Chapter 6: Conclusion serves as a brief summary of the chapters 2, 3, 4, and 5, concisely expressing the main points, results, and conclusion of this work.

# Chapter 2

## Methodology

Density functional theory (DFT) provides a mathematical framework to solve the fundamental equation of quantum physics called as “The many-body Schrödinger equation”. It is largely an *ab-initio* (first principles) approach, the objective of which is to predict properties of materials without taking any empirical or experimental input. The information of the constituent atoms alone is enough to compute and predict the properties of a material system quantum-mechanically. DFT can be used to find the physical, electronic, optical and magnetic properties of materials by modelling them as crystals, atomic clusters etc. It is also used to study chemical reactions and surface properties. Although lately, several new approaches like the stochastic quantum Monte Carlo methods and the wave function based methods in quantum chemistry (like the coupled-cluster method (CCSD)) have become popular due to their higher accuracy. DFT still has an upper hand, because it is quite computationally cheap and thus can be applied to systems containing several hundreds (even more!) of atoms. Moreover, over the years several excellent advancements have been made in making DFT more accurate and applicable to previously challenging systems like highly correlated systems etc.

### 2.1 The many-body Schrödinger equation

The many-body Schrödinger equation is an extension of the fundamental Schrödinger equation when applied to several particles. It describes many-electron systems like atoms, molecules and solids. Just like the fundamental single particle Schrödinger equation can describe a single particle like an electron in an arbitrary potential field, many-Body Schrödinger equation can describe the motion and the energies of a collection of particles like electrons and ions, in a complex potential field of the particles. Schrödinger equation is a fundamental equation in quantum mechanics, similar to Newton’s laws in classical mechanics. Newton’s laws can be used to predict the position and motion of particles being acted upon by external forces. Quite similarly, quantum mechanics (using Schrödinger equation) can be used to predict how the wave function of a particle (or several particles) will evolve in time and space when acted upon by an external potential field. The core difference between classical (Newton’s laws) and quantum mechanics (Schrödinger) is the uncertainty build in the quantum world, captured succinctly by the Heisenberg uncertainty principle. The best we can do is to predict how the quantum wave function of a system will evolve. The quantum wave function encodes information like the position in a probabilistic sense. The time dependent Schrödinger equation can be written as follows:

$$-\frac{\hbar^2}{2m}\nabla^2\Psi(\mathbf{r},t) + V(\mathbf{r})\Psi(\mathbf{r},t) = i\hbar\frac{\partial\Psi(\mathbf{r},t)}{\partial t}, \quad (2.1)$$

where the two terms on the left hand side of the equation represent kinetic energy and potential energy respectively.  $\psi(\mathbf{r},t)$  is the wave function of the system. It is a function of both space ( $\mathbf{r}$ ) and time ( $t$ ). However, many times we are not interested in how the quantum wave function will evolve in time. For example, in a steady-state system, we might be interested in the steady-state quantum wave function, given an arbitrary potential field. Moreover, transitions in the quantum world happen within fraction of seconds, and it is more important to obtain the steady-state quantum wave function. This is where the time independent Schrödinger equation becomes very important.

$$\frac{-\hbar^2}{2m}\nabla^2\psi(\mathbf{r}) + V(\mathbf{r})\psi(\mathbf{r}) = E\psi(\mathbf{r}) \quad (2.2)$$

The above equation can be rewritten as follows:

$$\left(\frac{-\hbar^2}{2m}\nabla^2 + V(\mathbf{r})\right)\psi(\mathbf{r}) = \hat{H}\psi(\mathbf{r}) = E\psi(\mathbf{r}) \quad (2.3)$$

The time independent Schrödinger equation now essentially becomes an eigenvalue problem.  $\hat{H}$  is called as the Hamiltonian.  $E$  represents the energy eigenvalues and  $\psi(\mathbf{r})$  represents the corresponding eigenvectors. The lowest energy eigenvalue is essentially the ground state energy of the system and the corresponding eigenvector is the ground state quantum wave function. Analytical solutions are possible only for very trivial systems like the Hydrogen atom and Hydrogen like atoms etc. Hence, solutions for practical systems are only possible numerically. This is why *ab initio* methods were developed. Numerous advancements in the field have led to calculations for systems containing several thousands of particles, which has advanced the field of physics, chemistry, and even microbiology [33, 34].

Consider a well-defined collection of atoms (like molecules or atoms in crystals). A key characteristic of this system of atoms is the energy of the electrons and ions, and how does it change when the constituent atoms move around. Suppose there are total  $N$  particles. Now, each particle has three spatial dimensions. This would make the wave function of this system as  $3N$  dimensional. Thus, we would have to solve the Schrödinger equation in  $3N$  dimensions. Even a small molecule like  $\text{H}_2\text{O}$  has 18 electrons, which means that the electronic wave function for this molecule would be 54 dimensional.

Atoms are composed of a heavier nucleus at the centre, surrounded by extremely light electrons. This fact is essential to split the problem of calculating energy into two parts: firstly the equation is solved for fixed nuclei, and the lowest energy configuration (ground state) for the electrons is calculated, followed by how the energy changes when the atoms or the ions move around. This approach of assuming the heavier nuclei to be fixed and thus splitting the original problem into two parts is called as the Born Oppenheimer approximation [1].

$$\left(\frac{-\hbar^2}{2m}\sum_{i=1}^N\nabla_i^2 + \sum_{i=1}^N\sum_{j<i}^N V(\mathbf{r}_i, \mathbf{r}_j) + \sum_{i=1}^N U(\mathbf{r}_i : \mathbf{R}_1, \mathbf{R}_2, \dots, \mathbf{R}_M)\right)\psi(\mathbf{r}) = E\psi(\mathbf{r}), \quad (2.4)$$

where  $V(\mathbf{r}_i, \mathbf{r}_j)$  is the potential from interacting electrons  $i$  and  $j$  and  $U(\mathbf{r}_i : \mathbf{R}_1, \mathbf{R}_2, \dots, \mathbf{R}_M)$  is the electron-ion potential. Using the Born Oppenheimer approximation, *ab initio* approaches treat



only electrons as quantum particles and the heavier ions (nuclei) are treated classically.

## 2.2 From wave functions to electron density

The wave function in itself is an abstract mathematical quantity. It is impossible to directly measure the wave function of a particle or a system of particles by any experimental means. The quantity that matters and can be measured is the electron density  $n(r)$  at a point in space. It is defined as:

$$n(r) = 2 \sum_i \psi_i(\mathbf{r})\psi_i^*(\mathbf{r}), \quad (2.5)$$

where  $\psi_i(\mathbf{r})$  represent the individual electron wave functions and  $\psi_i^*(\mathbf{r})$  are the complex conjugate of  $\psi_i(\mathbf{r})$ . The product of these two terms gives the probability of finding an individual electron in the wave function  $\psi_i(\mathbf{r})$  at position  $\mathbf{r}$ . The summation is multiplied by 2 to account for the fact that electrons have spin and thus according to Pauli's exclusion principle, each individual wave function can have two electrons with opposite spin. It is important to note that the electron density is a 3 dimensional quantity which is quite smaller than the  $3N$  dimensions of the many-body wave function.

## 2.3 The Hohenberg-Kohn theorems

DFT stands on two theorems proved by Kohn and Hohenberg. These theorems made solving the many-body Schrödinger equation computationally feasible in a consistent way. The theorems propose a departure from the wave function to electron density. In the book "Density Functional Theory: A Practical Introduction" by Sholl and Steckel, the first theorem is described as follows:

*"The ground state energy from Schrödinger equation is a unique functional of electron density" [1]*

In simple words, it means there is a one to one correspondence between the ground state energy and the electron density (i.e. ground state energy  $E$  can be expressed as  $E[n(\mathbf{r})]$ ). If the functional relationship is known, the electron density can be calculated and used to find the ground state energy. Electron density is much easier to compute than the complete multi-particle wave function. It reduces the complexity of computing the  $3N$  dimensional wave function to a 3 dimensional electron density. Hence, the first theorem makes it possible to solve the many-body Schrödinger equation (at least in principle), if the functional is known. The second theorem is summarized by Sholl and Steckel as:

*"The electron density that minimizes the overall functional is the true electron density corresponding to the full solution of Schrödinger equation"*

This is known as the variational principle. If the exact form of the functional is known, the true electron density can be easily calculated using this principle. However, the problem is that we do not know the exact form of the density functional. In practice, approximate functionals can be used to find out the electron density from which the ground state energy can be calculated.

## 2.4 Kohn-Sham equations

Kohn and Sham further showed that the task of calculating the true electron density using the variational principle is equivalent to solving a set of single particle Schrödinger equations representing the individual electrons of the system [35]. Single particle Kohn-Sham equation is written as:

$$\left( \frac{-\hbar^2}{2m} \nabla^2 + V(\mathbf{r}) + V_H(\mathbf{r}) + V_{XC}(\mathbf{r}) \right) \psi_i(\mathbf{r}) = \varepsilon_i \psi_i(\mathbf{r}), \quad (2.6)$$

where the first term in the Hamiltonian represents the kinetic energy of an electron,  $V(\mathbf{r})$  is the potential felt by an electron due to the collection of the atomic nuclei, and  $V_H(\mathbf{r})$  (Hartree potential) represents the Coulomb repulsion potential felt by an electron from the total electron density. It can be expressed as:

$$V_H(\mathbf{r}) = e^2 \int \frac{n(\mathbf{r}')}{|\mathbf{r} - \mathbf{r}'|} d^3 \mathbf{r}' \quad (2.7)$$

Hartree potential also includes an unphysical interaction of an electron with itself. This is called as the self-interaction error. The correction for this error is included in the final potential term  $V_{XC}(\mathbf{r})$  called as the exchange correlation term. The wave functions  $\psi_i(\mathbf{r})$  are called as the Kohn-Sham eigenvectors and  $\varepsilon_i$  are the corresponding Kohn-Sham eigenvalues. If the Kohn-Sham equations can be solved for single particle wave functions, those wave functions when multiplied by their complex conjugates and added together will give the electron density. The electron density can then be used to calculate the ground state energy and other interesting properties. However, there is a small problem. To solve the Kohn-Sham equations, firstly the potential terms in the Hamiltonian must be calculated. If we look at the second potential term (Hartree potential  $V_H(\mathbf{r})$ ), it depends upon the value of electron density. This means that to solve the Kohn-Sham equations for single particle Kohn-Sham states (and hence the electron density) we need the value of electron density beforehand. This problem can be solved if the Kohn-Sham equations are solved in a self-consistent way. This approach is used by all the DFT codes and is called as the Self Consistent Field (SCF) approach or calculation. Fig. 2.1 describes the normal workflow of self-consistent DFT calculations. It starts with guessing an initial electron density and then using it to calculate various potential terms in the Hamiltonian. We use the superposition of atomic charges as an initial guess for the electron density. This is followed by solving the Kohn-Sham equations for  $\psi_i(\mathbf{r})$ . A new electron density is then calculated from  $\psi_i(\mathbf{r})$ , the consistency of which is then checked against the initial guessed electron density. If self-consistency has been reached, the electron density can now be used to calculate other important quantities like forces, otherwise a new, electron density is generated and next iteration is started.

## 2.5 Basis set expansion and energy cutoffs

In quantum mechanics, wave functions are generally represented in terms of basis functions. Basis functions are simpler functions like gaussian or sinusoidal plane waves and a linear combination of basis functions can give the entire wave function. Larger basis set sizes generally give higher accuracy but with increased computational cost. Hence, it is necessary to strike a balance between computational cost and the accuracy for realistic production calculations. Complete basis set (CBS) limit can be achieved in practice by the extrapolation from multiple basis set sizes. However, generally in DFT calculations, a truncated basis set is used. In

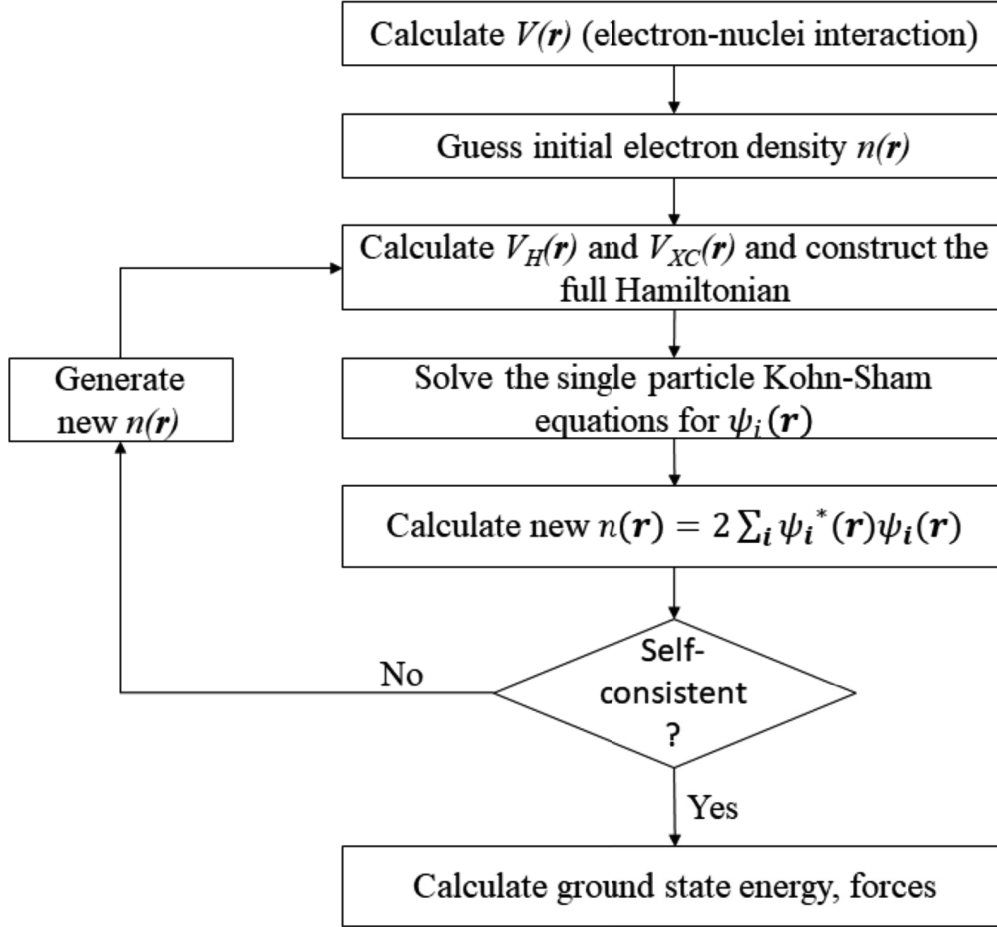


Figure 2.1: Workflow for a self-consistent solution of Kohn-Sham equations

quantum chemistry calculations for molecules, gaussian basis sets are widely used and in DFT calculations for periodic systems like crystals, slabs etc. plane wave basis sets are more commonly used.

For a periodic system, the solution of the Schrödinger equation satisfies a fundamental property known as the Bloch theorem [36]. It states that the solution can be expressed as a sum of the terms having the following form:

$$\phi_k(\mathbf{r}) = e^{i\mathbf{k}\cdot\mathbf{r}} u_k(\mathbf{r}), \quad (2.8)$$

where the exponential part represents plane waves with wave vector represented by  $k$  and  $u_k(\mathbf{r})$  is a periodic function with the periodicity of the unit cell or the supercell. Bloch's theorem essentially means that the Schrödinger equation can be solved for different  $k$  vectors independently.

Now since  $u_k(\mathbf{r})$  has the same periodicity as the cell, it can be written as a sum of special plane waves, which can be expressed as:

$$u_k(\mathbf{r}) = \sum_{\mathbf{G}} c_{\mathbf{G}} e^{i\mathbf{G}\cdot\mathbf{r}}, \quad (2.9)$$

where the summation is over all the reciprocal lattice vectors in the reciprocal space. The reciprocal lattice vectors are defined as:

$$\mathbf{G} = m_1 \mathbf{b}_1 + m_2 \mathbf{b}_2 + m_3 \mathbf{b}_3, \quad (2.10)$$

where  $\mathbf{b}_1$ ,  $\mathbf{b}_2$  and  $\mathbf{b}_3$  are the reciprocal basis vectors and  $m_i$  are integers. Combining equations 2.8 and 2.9 gives:

$$\psi_{\mathbf{k}}(\mathbf{r}) = \sum_{\mathbf{G}} c_{\mathbf{k}+\mathbf{G}} e^{i(\mathbf{k}+\mathbf{G})\mathbf{r}} \quad (2.11)$$

The above equation means that, the solution for even a single  $\mathbf{k}$  value requires a summation over an infinite number of vectors ( $\mathbf{G}$ ) in the reciprocal space which seems impossible. The solutions described by equation 2.11 are the solutions with kinetic energy:

$$E = \frac{\hbar^2}{2m} |\mathbf{k} + \mathbf{G}|^2 \quad (2.12)$$

An important point to consider here is that, the solutions with lower energy are more physically important than the solutions with high energies. This means that it is possible to truncate the infinite sum in equation 2.12 and include  $\mathbf{G}$  vectors of comparatively lower energies only. To achieve this, a parameter called as the cut off energy for plane wave expansion ( $E_{cut}$ ) is chosen and then used to truncate the infinite sum by calculating the cut off value for  $\mathbf{G}$  vectors ( $G_{cut}$ ) as follows:

$$E_{cut} = \frac{\hbar^2}{2m} G_{cut}^2 \quad (2.13)$$

The choice of  $E_{cut}$  is made through convergence tests. Various values of  $E_{cut}$  are used and the corresponding total energy of the system is computed. Generally, the total energy value starts to converge after a certain value of  $E_{cut}$ . This value of  $E_{cut}$  is finally chosen for the main production calculations. The convergence test done for anatase is shown in Fig. 2.2. Total energy only changes on the order of 0.01 eV after a cutoff value of 500 eV. The value  $\approx 0.01$  eV has been chosen as the tolerance value because it is well below the well defined value of chemical accuracy (1 kcal/mol or 0.043 eV). Similar convergence tests were also carried out for dopant atoms. We finally arrived at a value of 500 eV which has been used for all calculations.

## 2.6 $K$ points and Brillouin zone integrals

The real space coordinates can be converted into reciprocal space coordinates by using the Fourier transformation. The resultant space is also called as the  $k$ -space. It is generally efficient to perform certain calculations (specially integrals) in the reciprocal space. The concept of reciprocal lattice is also very useful in X-ray crystallography. Consider a crystal cell with lattice vectors  $\mathbf{a}_1$ ,  $\mathbf{a}_2$  and  $\mathbf{a}_3$ . The reciprocal lattice vectors are then defined as:

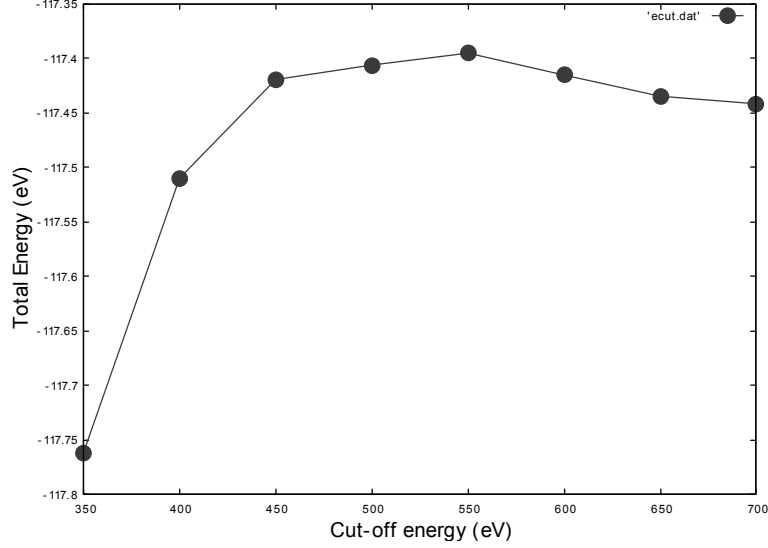


Figure 2.2: Convergence test for cutoff energy for anatase

$$\begin{aligned}
\mathbf{b}_1 &= 2\pi \frac{\mathbf{a}_2 \times \mathbf{a}_3}{\mathbf{a}_1 \cdot (\mathbf{a}_2 \times \mathbf{a}_3)} \\
\mathbf{b}_2 &= 2\pi \frac{\mathbf{a}_3 \times \mathbf{a}_1}{\mathbf{a}_2 \cdot (\mathbf{a}_3 \times \mathbf{a}_1)} \\
\mathbf{b}_3 &= 2\pi \frac{\mathbf{a}_1 \times \mathbf{a}_2}{\mathbf{a}_3 \cdot (\mathbf{a}_1 \times \mathbf{a}_2)}
\end{aligned} \tag{2.14}$$

The reciprocal lattice vectors are inversely proportional to the real space vectors. Thus, larger the real space lattice, smaller is the reciprocal space. Just like there is a primitive cell for every crystal in real space, the concept of primitive cell can also be extended to reciprocal space. Such a cell is called as the Brillouin zone. It is the smallest volume in the reciprocal space which can encode all the crystal information by utilizing crystal periodicity. Further, the Brillouin zone can be truncated further to give the irreducible Brillouin zone (IBZ) by taking advantage of the crystal symmetry. This further reduces the amount of computational resources required.

$K$  points represent the sampling points in the Brillouin zone. Technically speaking,  $\mathbf{k}$  represents the wave vectors of wave functions in a periodic supercell. The Schrödinger equation can be solved for each possible phase,  $\mathbf{k}$ , however the most general solution is found by integrating or summation over all values of  $\mathbf{k}$  as described by Bloch's theorem. Many observable quantities like energy of a state ( $E$ ) also require integration over  $\mathbf{k}$ . In all practical DFT calculations, a large portion of work is actually computing integrals of the form:

$$g = \frac{V_{cell}}{(2\pi)^3} \int_{BZ} g(\mathbf{k}) d\mathbf{k} \tag{2.15}$$

where  $g$  is a generic quantity to be computed and  $V_{cell}$  is the volume of the unit cell. This integral is defined in the reciprocal space and integrated over the possible  $\mathbf{k}$  values in the Brillouin zone. A Wigner-Seitz cell (primitive cell) in the reciprocal space defines the first Brillouin zone.

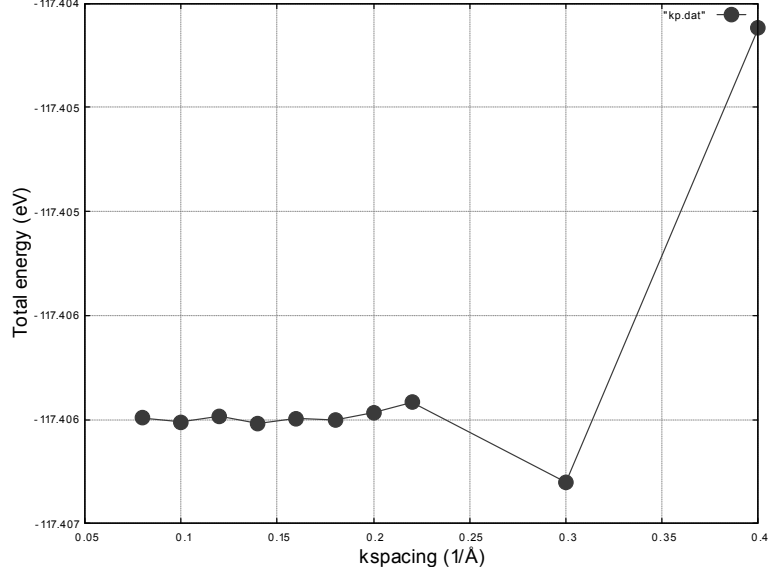


Figure 2.3: Convergence test for  $k$  spacing for anatase

To make the integral possible to compute, it is discretized by choosing a grid of  $k$  points. The discretization is also helped by the fact that the solutions to Schrödinger equation change slowly with respect to  $k$ , making the discretization possible. There are many ways of choosing the  $k$  point grid, but the most widely used method is the Monkhorst-Pack method in which the number of  $k$  points along each direction in the reciprocal space is specified, which are then placed uniformly by the DFT code to form a grid of  $k$  points [37]. Another approach is to specify  $k$  spacing, which is defined as the minimum allowed spacing between  $k$  points. If  $k$  spacing is reduced, the number of  $k$  points increases and vice-versa. The number of  $k$  points along the reciprocal lattice vectors are determined by the following:

$$N = \max\left(1, \frac{|\mathbf{b}_i|}{kspacing}\right), \quad (2.16)$$

where  $\mathbf{b}_i$  are the reciprocal vectors.  $N$  is rounded off to the next biggest integer. This approach has a slight advantage that only one parameter  $k$  spacing determines the  $k$  point grid, hence we only need to test this one parameter. Another inherent advantage is that the  $k$  points are distributed uniformly across the reciprocal lattice vectors. This approach was used in the current work. A  $k$  spacing value of  $0.20 \text{ \AA}^{-1}$  was used. Reducing the  $k$  spacing value further, changed the total energy only at the order of  $10^{-5} \text{ eV}$ . Hence, the  $k$  points grid was well converged (see Fig. 2.3).

## 2.7 Smearing

The smearing in DFT is necessary to avoid numerical instabilities during the self-consistent cycle. It is quite essential in case of a metallic system. Smearing imposes an artificial occupation of the Kohn-Sham states according to a smooth distribution, e.g. the Fermi distribution. Metallic systems have flat bands crossing the Fermi energy. Such bands may be completely occupied when below the Fermi energy and completely unoccupied when above it. During an SCF cycle, such bands may be completely occupied in one iteration and unoccupied in the next iteration.

This leads to large fluctuations in charge density and can stop us from achieving convergence. Hence, the electron occupations are smeared slightly near the Fermi energy. When required (for e.g. systems which showed metallic like nature), we used Gaussian smearing, with a small value (0.01 eV) of the smearing parameter (or the width of smearing). The smearing value should be taken as small as possible because it is an artificial imposition and can reduce the accuracy of DFT calculations.

## 2.8 Pseudopotentials

DFT is rarely used to do an all-electron calculation. An all-electron calculation means that the Kohn-Sham equations are solved for each and every electron in the system. This might be computationally expensive depending upon the scale of the system. Doing an all-electron calculation is not necessary most of the time because the electrons which are near the nuclei of atoms (core electrons) hardly take part in chemical bonding and reactions. It is the outer less tightly bound valence band electrons that play a major role in bonding and reactions. Pseudopotentials provide a way to separate the core electrons from the valence electrons. The electron density from the core electrons and the nuclear potential is replaced with a smoothed out potential (hence the name pseudopotential). This is called as the frozen core approximation. The Kohn-Sham equations are now solved for the valence electrons only and the effect of core electrons is included from the pseudopotential. This reduces the computational power required by a significant amount and the results are also quite close to an all electron calculation for most cases.

Pseudopotentials provide one more advantage. The electrons near the nucleus have high energies and rapidly oscillating wave functions. To represent these wave functions accurately much larger basis sets are required. Thus, by using pseudopotentials, the core electrons are excluded and the basis set convergence can be achieved at much lower energies. Numerous types of pseudopotentials are available and the choice of the pseudopotential depends upon the elements in the system and the properties of interest. The two most common types of pseudopotentials are the norm-conserving (NC) [38] pseudopotentials and the projector augmented wave (PAW) [39, 40]. The NC pseudopotentials generally have higher cutoffs than PAW types. In this work, PAW type pseudopotentials have been used for all the elements. The valence configuration specified by the pseudopotentials used are listed in Table. 2.1. All other electrons were considered as core electrons.

## 2.9 Exchange-correlation (XC) functionals

DFT is an *exact* theory in the sense that there exists an exchange-correlation functional that minimizes the ground state energy and reproduces the true ground state charge density. Unfortunately, however the true form of this functional is unknown. Some researchers in the field also believe that the exact functional even if found might be too complicated to implement computationally. The Hamiltonian as described in eq. 2.6 has known terms like the kinetic energy of electrons, electron-electron and electron-nucleus interaction terms. Exchange-correlation is the unknown part of the Hamiltonian. It plays a major role in all DFT calculations, as it determines the reliability of calculations, thus the choice of XC functional is very important.

Luckily, the XC functional can be computed for a homogeneous electron gas. However, systems of interest like crystals and molecules have widely varying electron density simply be-

Table 2.1: Valence configurations of various elements utilized in the current work

Element	Valence configuration
Ti	$3p^6 3d^3 4s^0$
O	$2s^2 2p^4$
Nb	$4p^6 5s^1 4d^4$
Ta	$5p^6 6s^1 5d^4$
V	$3p^6 3d^4 4s^1$
Mo	$4p^6 5s^1 4d^5$
W	$5p^6 6s^1 5d^5$
Cr	$3p^6 3d^5 4s^1$
La	$5s^2 5p^6 5d^1 6s^2$
Cu	$3p^6 3d^{10} 4s^1$
Co	$3d^8 4s^1$
Ce	$5s^2 5p^6 4f^1 5d^1 6s^2$

cause of the way charges are distributed within the materials. Even then, it provides a method to practically solve the Kohn-Sham equations. In this approach, the exchange-correlation potential ( $V_{XC}(\mathbf{r})$ ) at a point in the system (crystals and molecules) is taken to be the exchange-correlation potential computed for a homogeneous electron gas with the electron density same as the electron density at the point of interest in the system.

$$V_{XC}(\mathbf{r}) = V_{XC}^{egas}[n(\mathbf{r})], \quad (2.17)$$

where  $V_{XC}^{egas}[n(\mathbf{r})]$  is the exchange-correlation potential calculated for a homogeneous electron gas with electron density  $n(\mathbf{r})$ . This approach or approximation uses only the local electron density to compute the exchange-correlation potential. Hence it is called as the Local Density Approximation (LDA) [41]. It should be kept in mind that LDA is an approximation and using it does not truly solve the Schrödinger equation in an exact way. Still, LDA has proved to be very useful in solving the Kohn-Sham equations for real systems.

Generalized Gradient Approximation (GGA) is another class of functionals which is widely used [42]. It goes beyond LDA by using not only the local electron density but also its gradient to compute the exchange-correlation potential. It is generally more reliable than the LDA and has been used in the current work. There are several types of GGA functionals like the Perdew-Burke-Ernzerhof functional (PBE) [43] and the Perdew-Wang functional (PW91) [44] depending upon the way they include the electron density gradient in the functional. GGA-PBE XC functional has been used for the majority of calculations in the current work.

LDA and GGA are quite successful for predicting properties of a wide variety of systems, but they still fail for certain quantum systems. There are certain cases like transition metal oxides, graphene etc. where the failure of LDA and/or GGA is well documented [45, 46]. For semiconductors, these functionals systematically underestimate band gaps by approximately 50-100%. This is known as the band-gap problem [47]. DFT with conventional XC functionals also fails in systems with localized  $d$ (transition metal oxides) or  $f$  electrons (rare-earth oxides) [47]. LDA and GGA tend to delocalize the electrons over the entire crystal in these cases.



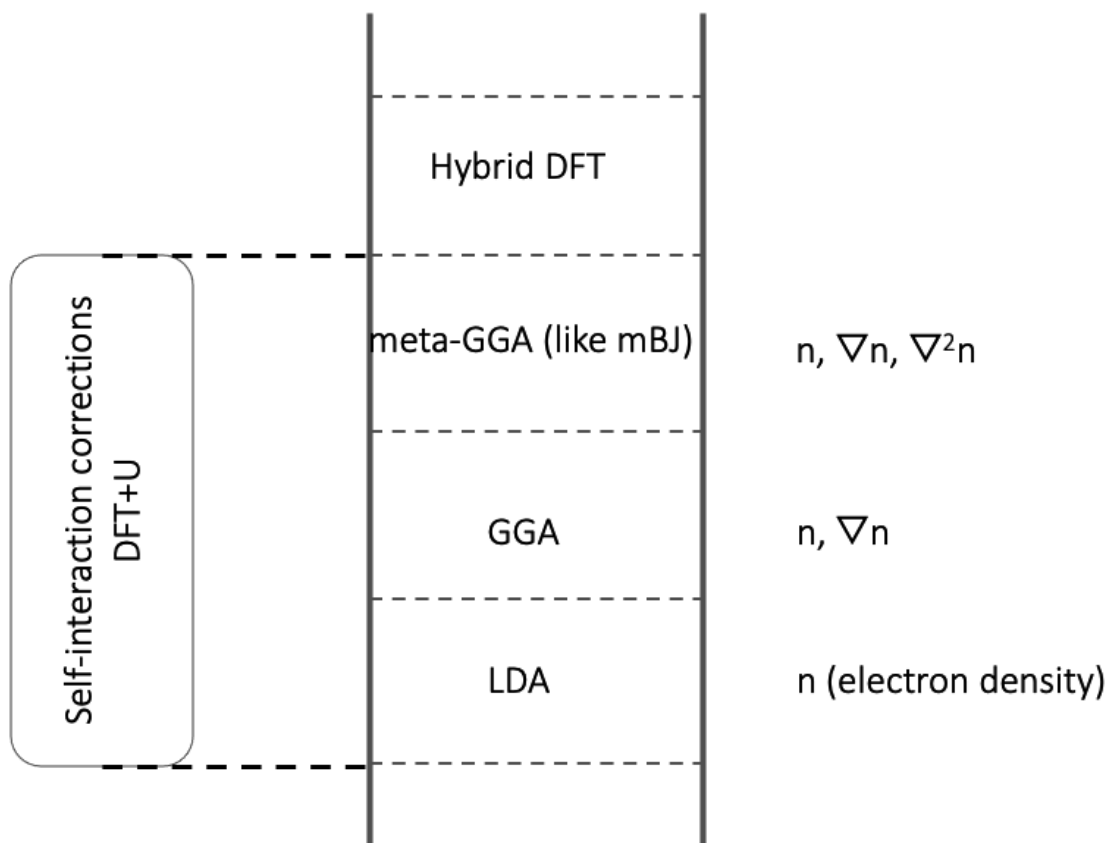


Figure 2.4: Jacob's ladder of DFT functionals (adapted from Sholl *et al.* [1])

To mitigate the shortcomings of LDA and GGA, several new approaches/functionals have been devised. One such approach is using hybrid exchange-correlation functionals. Hybrid functionals basically incorporate more accurate short range exact exchange (from Hartree-Fock calculation) with the rest of the XC energy. They interpolate between band-gap underestimation with GGA and its overestimation at the Hartree-Fock level [47]. They have been successfully applied to many materials [48], where GGA and LDA give incorrect results. However, hybrid functionals introduce additional empirical parameters (like the mixing parameter for mixing short and long exchange) for which a choice has to be made. These parameters might be tuned to give accurate properties for a certain material, but then the approach loses its prediction ability. These functionals also increase the computational cost significantly.

The GGA functional can be further improved upon by including the local gradient expansion upto second derivatives or even higher. This gives meta-GGA functionals. A popular meta-GGA functional is the modified Becke-Johnson (MBJ) functional [49, 50]. It combines the exchange part of the MBJ potential with LDA or GGA correlation potential. The exchange part consists of terms whose weights are controlled by an empirical parameter  $c$ . MBJ can yield better band gaps which is also evident from the current work, but the tuning of  $c$  parameter reduces predictability.

Another approach is to include a simple correction term to the conventional XC functional. It has successfully been applied to several strongly correlated materials [51, 52]. This correction term is referred to as the Hubbard correction and is described in the next section in detail.

Fig. 2.4 shows the “Jacob’s ladder” of DFT functionals. As we go towards the top, it is expected that we reach closer and closer to the “true functional”.

## 2.10 Hubbard $U$ correction (DFT+ $U$ )

Hartree potential that describes Coulomb repulsion (eq. 2.7) between an electron and total electron density includes by definition an unphysical interaction between an electron and itself, called as self-interaction. The associated energy is called as the self-interaction energy. Due to incomplete cancellation of the self-interaction energy (due to approximate nature of DFT functionals), error arises. Self-interaction error causes highly localized orbitals to be improperly destabilized. Strongly correlated materials like the transition metal oxides are often poorly described with local and semi-local functionals like LDA and GGA due to the self-interaction error. Unpaired localized electrons tend to delocalize in order to minimize the self-interaction. For example, a class of materials called as Mott insulators are predicted by LDA or GGA as metals. One of the simplest solutions found by researchers to solve this problem is to use the Hubbard correction term  $U$  [52]. This method introduces a single parameter  $U_{eff}$  that corrects the electron self-interaction.

### 2.10.1 Determining the Hubbard $U$ parameter using the linear response approach

In this section, the scheme to determine  $U_{eff}$  for Ti is described. For a rigorous derivation, we refer the reader to the original paper [31]. The basic idea is to compute the self-consistent and the non self-consistent linear response functions. Non self-consistent response can be written as:

$$\chi_{IJ}^0 = \frac{\partial N_1^{NSCF}}{\partial V_J} \quad (2.18)$$

The above response function quantifies the change in the number of  $d$  orbital electrons on a site  $I$  due to a spherical potential perturbation acting on  $d$  orbital at site  $J$ . The response is defined only when  $I \neq J$  and is 0 otherwise. Similarly, the self-consistent response is defined as:

$$\chi_{IJ}^0 = \frac{\partial N_1^{SCF}}{\partial V_J} \quad (2.19)$$

Now, the Hubbard parameter is given by:

$$U_{eff} = \left( \frac{\partial N_1^{SCF}}{\partial V_J} \right)^{-1} - \left( \frac{\partial N_1^{NSCF}}{\partial V_J} \right)^{-1} \quad (2.20)$$

Both the response functions are computed for a series of potential perturbations. Response functions are then easily computed by linear fitting the number of  $d$  electrons as a function of perturbation potential  $V$ . The fitting process for Ti is shown in Fig. 2.5

$$U_{eff} = \frac{1}{0.114} - \frac{1}{0.291} = 5.29eV \quad (2.21)$$

$U_{eff}$  calculated for all the dopants is listed in Table. 2.2.

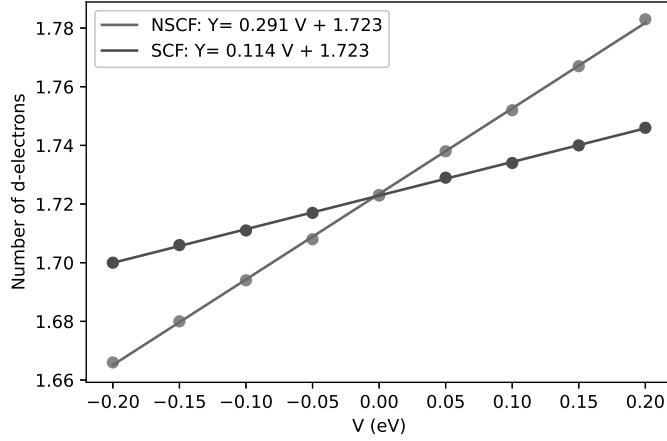


Figure 2.5: Linear fitting of  $d$  orbital occupation for the Ti site in  $\text{TiO}_2$

Table 2.2:  $U_{eff}$  values of various elements computed using Linear response method

Element	$U_{eff}$ (eV)
Ti (d)	5.23
Ta (d)	3.5
Nb (d)	1.21
Mo (d)	2.9
W (d)	4.08
Cr (d)	5.78
V (d)	8.02
La (d)	2.19
Cu (d)	8.68
Co (d)	7.05
Ce (f)	6.62

## 2.11 Formation energy of point defects

Comparing the formation energy of defects can give useful information like which defects are more likely to form, which defects can form spontaneously and which cannot. To compare and understand the relative stabilities of various defects, formation energy ( $E^f[X^q]$ ) was calculated using the following equation:

$$E^f[X^q] = E_{tot}[X^q] - E_{tot}[bulk] - \sum_i n_i \mu_i + qE_F, \quad (2.22)$$

where  $E_{tot}[X^q]$  is the total energy of the supercell with defect  $X$ ,  $E_{tot}[bulk]$  is the total energy of an equivalent defect free supercell,  $n_i$  represents the number of atoms of type  $i$  that have been added to or removed from the supercell to create the defect,  $\mu_i$  represents the chemical potential of the defect forming species (Ti or O),  $q$  represents the charged state of the defect and  $E_F$  is the Fermi level referenced to the valence band maxima (VBM) in the bulk. To calculate the

chemical potential of Ti and O in Ti or O rich conditions, the following boundary criteria were considered:

$$\begin{aligned}\mu_{Ti} + 2\mu_O &= \mu_{TiO_2,bulk}, \\ \mu_{Ti} &\leq \mu_{Ti,bulk}, \\ \mu_O &\leq \frac{\mu_{O_2molecule}}{2},\end{aligned}\tag{2.23}$$

where  $\mu_{Ti}$  and  $\mu_O$  are the chemical potentials of the defect forming species of Ti and O respectively.  $\mu_{TiO_2,bulk}$ ,  $\mu_{Ti,bulk}$  and  $\mu_{O_2molecule}$  respectively. Note that, here the total energies were calculated for each of these structures per formula unit, which were then used as their chemical potential values. Moreover,  $\mu_{Ti}$  and  $\mu_O$  should always be lower than their natural phases of  $\mu_{Ti,bulk}$  and  $\mu_{O_2molecule}$  respectively, otherwise these natural phases of Ti and O<sub>2</sub> would form instead of TiO<sub>2</sub>. For O-rich conditions,  $\mu_O = \frac{\mu_{O_2molecule}}{2}$  and for O-poor conditions,  $\mu_{Ti} = \mu_{Ti,bulk}$ .

## 2.12 Force calculation and geometry optimization

DFT calculations can be used to predict the lattice parameters and atomic positions of a system. This is because DFT allows calculation of forces using the Hellman-Feynman theorem [53]. From self-consistent cycles of DFT, the eigenvalue  $E$  and the eigenfunctions  $\phi(\mathbf{r})$  can be computed. Then other observables like atomic forces can be computed.

$$\frac{\delta E}{\delta x} = \left\langle \psi(x) \left| \frac{\delta \hat{H}}{\delta x} \right| \psi(x) \right\rangle\tag{2.24}$$

Atomic forces are given by the derivative of energy with respect to  $\mathbf{r}$ . A standard geometry optimization includes several SCF loops.

Forces and stresses are calculated at the end of each SCF loop and based on that the atomic parameters are perturbed for the next SCF loop using an algorithm. Conjugate-gradient algorithm was used to update the ionic positions during geometry optimization in this work.

## 2.13 Effective masses of charge carriers

Semiconductors show interesting behaviour when external perturbations like electric field, temperature or stress are applied. In a crystal, electrons interact with a periodic potential and the response of the electrons to a perturbation, depends upon how electrons interact with this periodic potential. Electrons don't act like classical particles inside atoms but as quantum particles. However, they can be approximated as free electrons having a renormalised mass. This renormalised mass is called as the "effective mass". It is important to note here that effective mass of electron and its rest mass are not the same. Effective mass encodes the interaction of electrons as quantum particles with the periodic potential of the crystal and its value is not constant. Effective masses can also be computed for holes just like electrons. Accurate calculation of effective masses from the band structure of materials helps in predicting and understanding the electronic, optical and transport properties of semiconductors. Python package "effmass" was used to compute effective masses of charge carriers [54].

Effective mass can be computed in several different ways from the band dispersion  $E(k)$ , ob-

tained from a DFT calculation. In ideal case, the bands are perfectly parabolic and the effective mass values computed using different definitions are all equal. However, in real materials, the bands are non-parabolic, and this leads to different values of effective masses of charge carriers based on the algebraic definition used to compute them. Various definitions of effective mass are shown in the schematic Fig. 2.6.

### 2.13.1 Curvature effective mass

This is the conventional definition of effective mass.

$$\frac{1}{m_c} = \frac{1}{\hbar^2} \frac{\partial^2 E}{\partial k^2}, \quad (2.25)$$

where  $m_c$  is the curvature effective mass. The term  $\frac{\partial^2 E}{\partial k^2}$  indicates the curvature of the bands and can be computed from the band dispersion or band structure from DFT calculation. Thus, higher the curvature of bands, lower is the value of effective mass and vice-versa. This means that flatter bands (low curvatures) have higher effective masses. The expression for curvature effective mass (eq. 2.25) is derived using Newton's second law [55, 56], hence it is also called as the inertial effective mass. It is also sometimes called as the conductivity effective mass because it effectively describes the "acceleration" of an electron in an applied electric field. When we are interested in dispersion of eigenstates near the conduction and valence band edges, the band dispersion can be approximated as parabolic.

$$E(k) = \frac{\hbar^2 k^2}{2m_c} \quad (2.26)$$

The curvature effective mass can be calculated in several ways. All the definitions of curvature effective mass will give the same value only if the bands are perfectly parabolic.

#### Finite difference effective mass

A three point finite difference equation was used to calculate the curvature of the band at point  $i$ .

$$\frac{\partial^2 E}{\partial k^2} = \frac{E_{i+2} - 2E_{i+1} + E_i}{|k_{i+1} - k_i|^2}, \quad (2.27)$$

where  $k_i$  is a point in the reciprocal space and  $E_i$  is the energy eigenvalue at that point.  $E_{i+1}$  is the next eigenvalue and so on.

#### Unweighted least-squares fitting

The parabolic dispersion is given by the formula:

$$E = ck^2 \quad (2.28)$$

To obtain the coefficient  $c$  the dispersion was fitted using least-squares method by minimising the residuals:

$$\sum_{i=1}^5 (ck_i^2 - E_i)^2 \quad (2.29)$$

Five points from the band dispersion were used for fitting.

### Weighted least-squares fitting

The following sum of squared residuals can be minimized:

$$\sum_{i=1}^n W_i (ck_i^2 - E_i)^2 \quad (2.30)$$

The summation was done over an energy range of 0.25 eV. All the points in the band dispersion within this energy range were considered. Their weights were calculated from the Fermi-Dirac distribution:

$$W_i(E_i, T) = \frac{1}{\exp\left(\frac{E_i - E_F}{k_B T}\right) + 1}, \quad (2.31)$$

where  $E_F$  is Fermi energy and  $k_B$  is the Boltzmann's constant and  $T$  is the temperature.

### 2.13.2 Transport effective mass

At high temperatures or at higher carrier concentrations, eigenstates far from the band extrema (non-parabolic nature) are accessed. To account for non-parabolic nature of bands, wave-particle duality for an electron wavepacket can be used to derive the following formula for transport effective mass [56].

$$\frac{1}{m_t} = \frac{1}{\hbar^2 k} \frac{\partial E}{\partial k} \quad (2.32)$$

### 2.13.3 Kane quasi-linear dispersion

To account for non-parabolic bands another approach is to include the non-linear terms and expand eq. 2.26 as follows:

$$\frac{\hbar^2 k^2}{2m_{t,edge}} = E + \alpha E^2 + \beta E^3 + \dots, \quad (2.33)$$

where  $m_{t,edge}$  is the transport effective mass at the band edge (or Kane mass). If degree 3 and higher terms are neglected, Kane quasi-linear dispersion relation can be obtained [57].

$$\frac{\hbar^2 k^2}{2m_{t,edge}} = E(1 + \alpha E), \quad (2.34)$$

where the  $\alpha$  parameter specifies the non-parabolic nature of bands. If the bands are perfectly parabolic,  $\alpha = 0$ . For conduction bands in general  $\alpha$  is positive, and it is negative for holes in valence bands. Differentiating the kane dispersion w.r.t  $k$  gives the transport effective mass as:

$$m_t(E) = m_{t,edge}(1 + 2\alpha E) \quad (2.35)$$

### 2.13.4 Optical effective mass

Optical effective mass is defined as:

$$\frac{1}{m_{opt}} = \frac{2}{n_e} \sum_l \sum_k^{occ.} \frac{1}{m_c^l(k)}, \quad (2.36)$$

where  $m_{opt}$  is the optical effective mass,  $n_e$  is the charge carrier concentration and  $m_c^l$  is the curvature effective mass for a band  $l$  and an occupied eigenstate  $k$ . Optical effective mass incorporates summation over all occupied eigenstates and each band  $l$ . This can account for non-parabolicity in bands. According to a derivation by Huy *et al.* [58], the summation can be replaced by an integration along one-dimensional paths in the  $k$ -space:

$$\frac{1}{m_{opt}} = \frac{\sum_l \int f(E, T) \frac{\partial^2 E}{\partial k^2} dk}{\sum_l \int f(E, T) dk} \quad (2.37)$$

where  $f(E, T)$  represents the Fermi-Dirac distribution.

Since band dispersions are rarely parabolic for real materials, Kane dispersion is more accurate. The computed transport and optical effective masses depend upon the charge carrier energy. When through doping, or increasing temperature etc. the bands are progressively filled the effective mass also changes (generally increases [59]). This also changes properties like charge carrier mobility. The amount of change in optical and transport effective masses with respect to carrier concentration depends upon the non-parabolicity of bands. It should be noted here that, the curvature effective mass does not depend upon carrier concentration and is defined by band curvatures alone. Since optical effective mass incorporates band non-parabolicity it has been used as an important parameter for design of transparent conducting oxides [60].

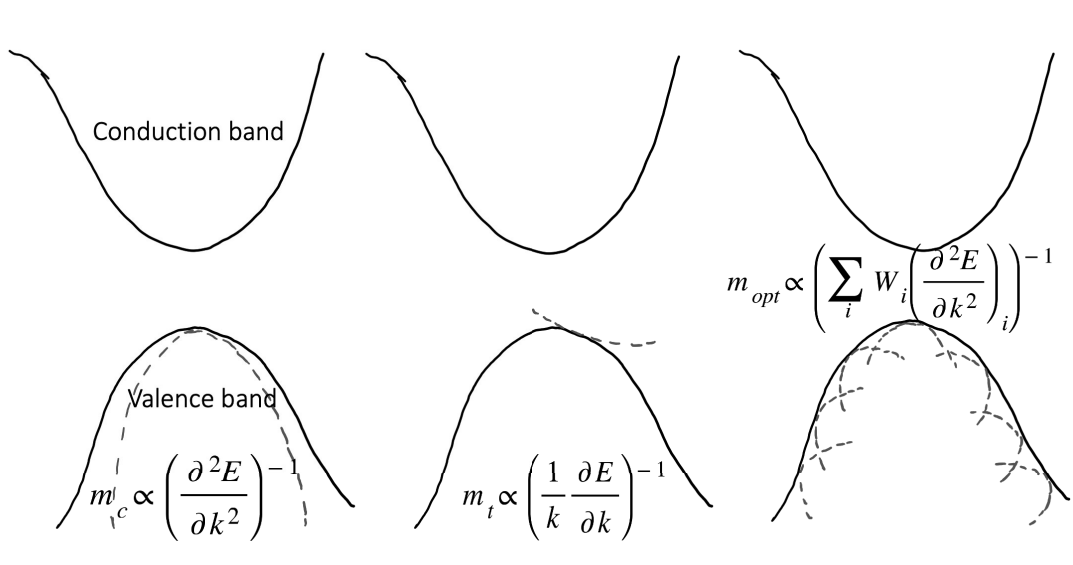


Figure 2.6: Curvature, transport and optical effective mass

# Chapter 3

## Pristine Anatase

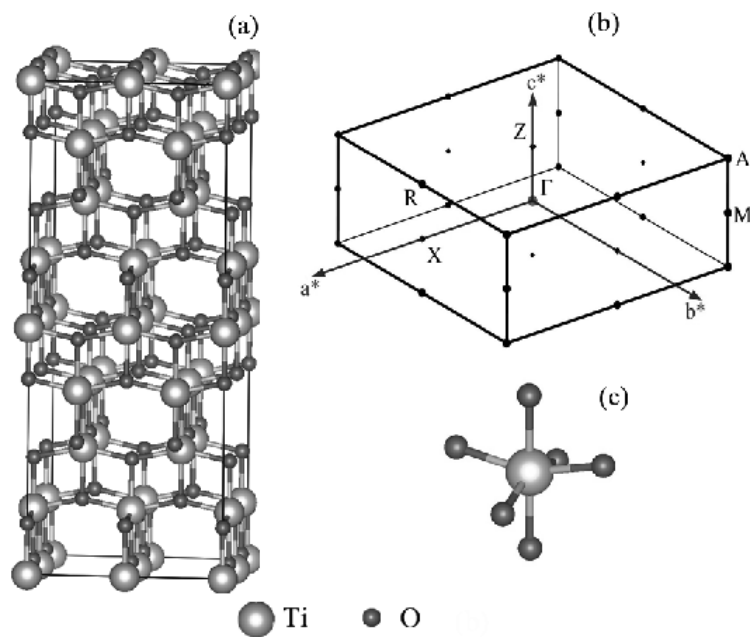


Figure 3.1: Schematic of (a) anatase supercell, (b) the first Brillouin zone of anatase lattice with high symmetry  $k$  points and (c) distorted TiO<sub>6</sub> octahedron of anatase. The two vertical Ti-O (apical) bonds are slightly longer than the other four equatorial Ti-O bonds.

*Ab initio* calculations for pristine anatase, anatase with intrinsic defects and doped anatase were performed using Quantum ESPRESSO [61] and VASP [62–65] software packages. Convergence tests and parameter calculations were first carried out as discussed in Chapter 2. This was followed by geometry optimization for all the structures (including both cell parameters and atomic positions optimization) using the conjugate gradient algorithm. This relaxed (optimized) structure was then used for self-consistent field (scf) and band structure (non-scf) calculations. The curvature of the band structure was then used to calculate the effective masses of charge carriers.



### 3.1 Lattice and electronic structure

Pristine anatase has a tetragonal structure. It consists of distorted  $\text{TiO}_6$  octahedron as its building block. The computed lattice parameters, bond lengths, band gap and bader atomic charges [66, 67] are shown in Table 3.1. Computations were performed for two values of  $U$  parameter, 4.2 eV and 5.29 eV. The former value has been used in literature to calculate the lattice parameter, bulk modulus and defect states of surface oxygen vacancies in anatase using DFT (GGA)+ $U$  approach, and the calculated data were found to be in agreement with those of the experimental results and/or those calculated using the hybrid DFT route [68, 69]. The latter value was determined using linear response *ansatz* as discussed in 2. The computed values are compared with both theoretical and experimental values available in the literature. The lattice parameters  $a$  and  $b$  and the Ti-O bond lengths are in excellent agreement with previous experimental and computational estimates. However, there is a small discrepancy in case of the lattice parameter  $c$ . The computed lattice parameters depend slightly on the pseudopotential and the exchange-correlation functional used for the computation. Labat *et al.* performed a thorough investigation of the dependence of lattice parameters of anatase on the computational methodology (pseudopotential + xc). They discovered that the lattice parameters  $a$  and  $b$  were largely independent of the computational methodology used, and the associated error was within  $\pm 1\%$ . However for  $c$ , the dependence on computational methodology was noticeable. It was found to be systematically overestimated by about 4% with respect to experimental data [70]. The current results are consistent with their findings. The overall agreement of structural parameters with the existing computational and experimental reports indicates the reliability of the methodology used in this work in predicting electronic defect states for anatase. The average bader charges [66, 67] on Ti and O atoms also agree with previous literature reports. The charges computed using  $U = 5.29$  eV are more accurate.

The band structure and the DOS plots for anatase are shown in the Fig. 3.2. The band structure shows an indirect band gap of 2.44 eV ( $U = 4.2$  eV) and 2.72 eV ( $U = 5.29$  eV) which is an underestimation even after Hubbard  $U$  correction. Clearly, the larger  $U$  value opens up the gap more and the band gap value is closer to those obtained using mBJ-GGA and mBJ-LDA [77]. It should be noted here that, mBJ is a potential-only functional. It takes the exchange-correlation term from GGA or LDA. This in turn means that mBJ calculations are not self-consistent with respect to energy. Thus, it is not possible to compute ionic forces (ionic relaxation not possible). Even though mBJ for some systems gives better prediction of band gaps, the relative positions of defect states remains unchanged. These are the reasons GGA+ $U$  has been chosen for the current study.

Table 3.1: Lattice parameters, bond lengths (in Å), band gap (in eV) and Bader charges for anatase.

	Methodology	Lattice parameters		Ti-O bond lengths		Band gap	Bader charges	
		a=b	c	Apical	Equatorial		Ti	O
Current work	GGA+ $U$ (4.2 eV)	3.84	9.84	1.99	1.95	2.44	+2.25	-1.15
	GGA+ $U$ (5.29 eV)	3.87	9.77	2.02	1.98	2.72	+2.41	-1.21
						2.6 (mBJ-GGA) 2.8 (mBJ-LDA)		
Other computational work	GGA <sup>a</sup>	3.81	9.63	—	—	2.14	—	—
	GGA+ $U$ <sup>b</sup>	3.83	9.63	2.00	1.96	2.00	—	—
	GGA+ $U$ <sup>c</sup>	3.82	9.55	—	1.95	2.61	—	—
	Full-potential all-electron calculation (PBE) <sup>d</sup>	3.81	9.72	2.01	1.95	—	+2.50	-1.30
Experimental value <sup>e,f</sup>		3.78	9.50	1.98	1.93	3.21	—	—

<sup>a</sup> Reference 71; <sup>b</sup> Reference 72; <sup>c</sup> Reference 73; <sup>d</sup> Reference 74; <sup>e</sup> Reference 75; <sup>f</sup> Reference 76;

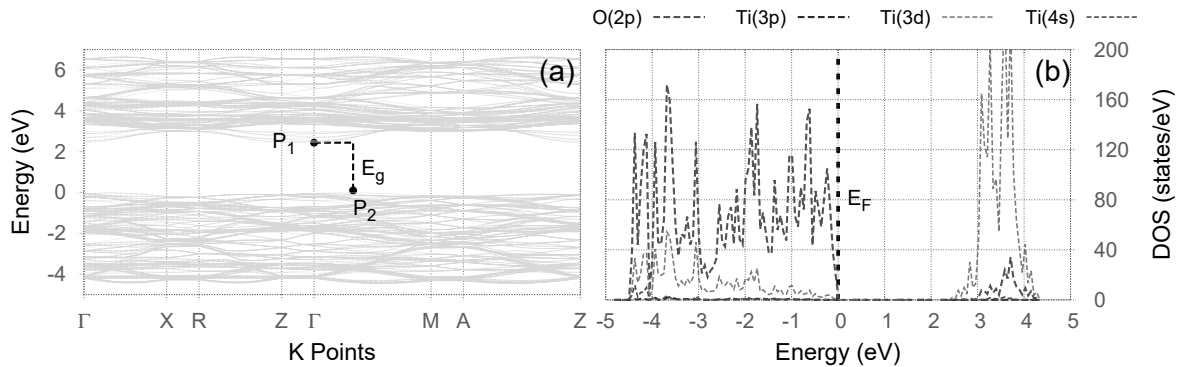


Figure 3.2: Band structure (a) and PDOS (b) of anatase. Points  $P_1$  and  $P_2$  correspond to the CBM and VBM respectively and  $E_g$  is the indirect band gap (2.44 eV). Fermi energy ( $E_F$ ) has been shifted to 0 eV.

# Chapter 4

## Intrinsic Defects

The intrinsic (or native) defects considered were oxygen vacancies ( $V_O$ ), oxygen interstitials ( $O_i$ ), titanium vacancies ( $V_{Ti}$ ) and titanium interstitials ( $Ti_i$ ). The reported  $U$  value of 4.2 eV [68,69] for Ti  $d$  electrons was used.

### 4.1 Geometrical distortion due to native defects

The bond lengths of the anatase crystal were found to be altered because of the creation of native defects, thus creating a geometrical distortion in the vicinity of the defect sites (see Table. 4.1). The directions of forces acting on the atoms near the defect site are shown in Fig. 4.1.

$V_O$  formed three dangling Ti-O bonds (see Fig. 4.1(a)). The three Ti atoms in the neighbourhood moved outwards from the defect site due to their mutual strong repulsion, which could be attributed to the positive charge (or oxidation state) on Ti atoms. The two nearby O atoms moved towards the defect site, possibly to minimize the total energy of the system.

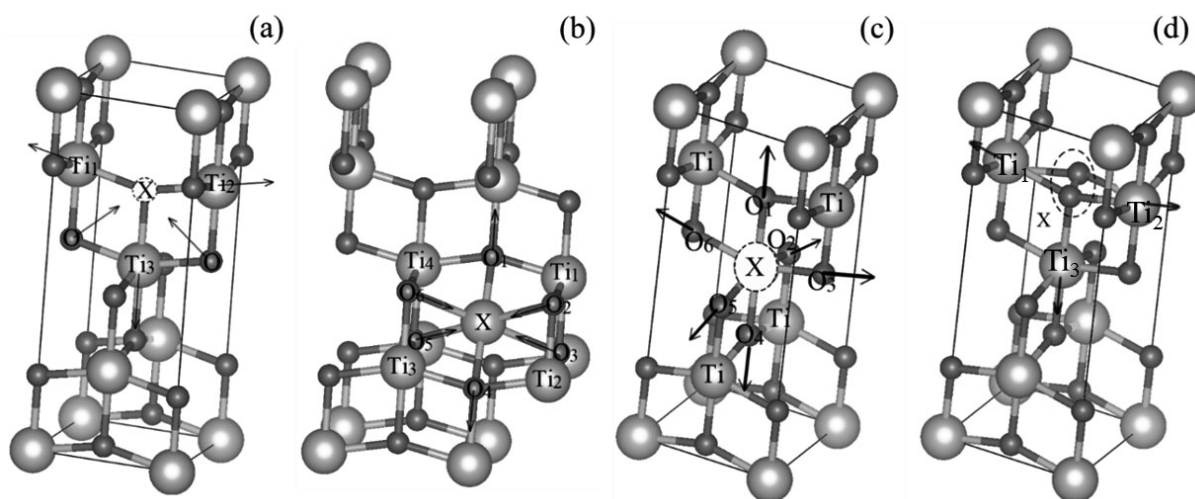


Figure 4.1: A conventional cell of anatase showing the direction of forces acting on the neighbouring atoms to the defect site (called as the defect associated atoms). The defect site has been marked as X. The figures depict anatase with (a) $V_O$ , (b) $Ti_i$ , (c) $V_{Ti}$  and (d) $O_i$  respectively.

Usually in previous literature reports,  $Ti_i$  has been placed at the centre of the distorted octahedron formed by the oxygen atoms in the anatase lattice [25]. However, we used two

Table 4.1: Distances ( $\text{\AA}$ ) of the defect associated atoms from the defect site

	Atomic distances from defect site X													
	X = $V_O$				X = $Ti_i$				X = $V_{Ti}$				X = $O_i$	
	X-Ti <sub>1,2</sub>	X-Ti <sub>3</sub>	X-O	X-O <sub>1,4</sub>	X-O <sub>2,3,5,6</sub>	X-Ti <sub>1-4</sub>	X-O <sub>1,4</sub>	X-O <sub>2,3,5,6</sub>	X-Ti	X-Ti <sub>1</sub>	X-Ti <sub>2</sub>	X-Ti <sub>3</sub>		
Undistorted lattice	1.95	1.99	2.48	1.84	2.25	2.42	1.99	1.95	3.06	1.95	1.99	1.95		
Distorted lattice	1.97	2.10	2.41	2.02	2.10	2.65	2.47	2.02	2.95	1.97	2.05	2.12		

initial structures in our calculations, to find the more stable anatase structure with  $Ti_i$ . In the former, the interstitial atom was placed at a random location inside the crystal (position X in Fig. 4.1(b)) and allowed to reach its lowest energy configuration by using atomic relaxation. In the latter approach, the total energy calculation for anatase with  $Ti_i$  at the centre of the distorted octahedron was performed. The total energy of the first configuration was found to be slightly lower (by 0.23 eV) than that of the second one, suggesting higher stability of the first configuration over the second one. Hence, only the first configuration was used for all further calculations. The Ti atoms near the interstitial  $Ti_i$  atom (Ti<sub>1</sub>, Ti<sub>2</sub>, Ti<sub>3</sub> and Ti<sub>4</sub>) were found to move away from the defect site due to the mutual repulsion among Ti atoms (see Table 4.1). The two O atoms present at the apical positions (i.e., O<sub>1</sub> and O<sub>4</sub> in Fig. 4.1(b)) were found to move outwards from the interstitial site. However, the other four oxygen atoms surrounding the defect site (i.e., O<sub>1</sub>, O<sub>3</sub>, O<sub>5</sub> and O<sub>6</sub>) were found to be attracted and move towards this interstitial site (see Table 4.1).

$V_{Ti}$  resulted in the six oxygen atoms in the neighbourhood (i.e., O<sub>1</sub>-O<sub>6</sub>), which were found to relax outwards due to their strong mutual repulsion (see Fig. 4.1(c) and Table 4.1). Here, the oxygen atoms present at the apical positions (i.e., O<sub>1</sub> and O<sub>4</sub>) were found to relax outwards farther ( $\approx 0.5\text{\AA}$  away from  $V_{Ti}$ ; see Table 4.1) than those present at non-apical positions. Ti atoms surrounding the defect site were found to be displaced inwards only slightly, probably because of the missing repulsive force from the removed Ti atom.

Introducing  $O_i$  in anatase led to the formation of a dimer configuration with that of the lattice oxygen atom (see Fig. 4.1(d)). Note that, relaxation of atomic positions automatically resulted into this configuration even when we did not assume  $O_i$  to form a dimer with a lattice oxygen atom. The O-O bond length of the dimer was found to be  $1.47\text{\AA}$ , which is close to the O-O bond length in  $[O_2]^{2-}$  as calculated for BaO<sub>2</sub> ( $1.49\text{\AA}$ ), indicating the existence of the dimer in the form of  $[O_2]^{2-}$  [78]. The geometry around the defect site was only found to be slightly affected, with the neighbouring Ti atoms (Ti<sub>1</sub>, Ti<sub>2</sub>, Ti<sub>3</sub>) found to move slightly outwards (see Table 4.1).

## 4.2 Neutral and charged oxygen vacancies ( $V_O$ , $V_O^{+1}$ , $V_O^{+2}$ )

$V_O$  in anatase would create dangling bonds and two unpaired electrons in its vicinity due to the valence state of two on an O atom. The DOS plots of anatase with various charged states of O vacancy clearly showed the formation of a mid-gap defect state (see Fig. 4.2). This gap state was found to spread over a narrow energy range, indicating it to be highly localized (flat bands). Moreover, DOS plot of anatase with  $V_O$  clearly showed the defect state being associated to Ti  $3d$  orbitals, suggesting the states being localized on a few Ti atoms surrounding the defect site (see Fig. 4.2(b)). In this case, Fermi energy was found to lie at the edge of the gap state on the side of the conduction band, indicating this mid-gap state being occupied. Whereas, for  $V_O$  the defect states were found to form 0.56 eV below the conduction band edge, the gap states were found to

move closer to the conduction band edge with increasing positive charge on the vacancy from 0 to +2 (see Fig. 4.2(b)-(d)) The gap state became very close to the conduction band edge ( 0.07 eV) for anatase with  $V_O^{+1}$ . Additionally,  $E_F$  in this case was found to be positioned around the middle of the defect state (see Fig. 4.2(c)). Thus, electrons in the gap state could excite to the conduction band and thereby providing  $n$ -type conductivity to anatase. For anatase with  $V_O^{+2}$ , the defect state was found to form inside the conduction band near the CBE (seen as a distinct peak at CBE in Fig. 4.2(d)) with  $E_F$  being located at the VBM. The band gap values for anatase with  $V_O$ ,  $V_O^{+1}$  and  $V_O^{+2}$  were found to be 2.55 eV, 2.48 eV and 2.35 eV respectively. The reduced band gap of anatase with  $V_O^{+2}$  could be attributed to the formation of the defect states close to the conduction band edge (see Fig. 4.2(d))

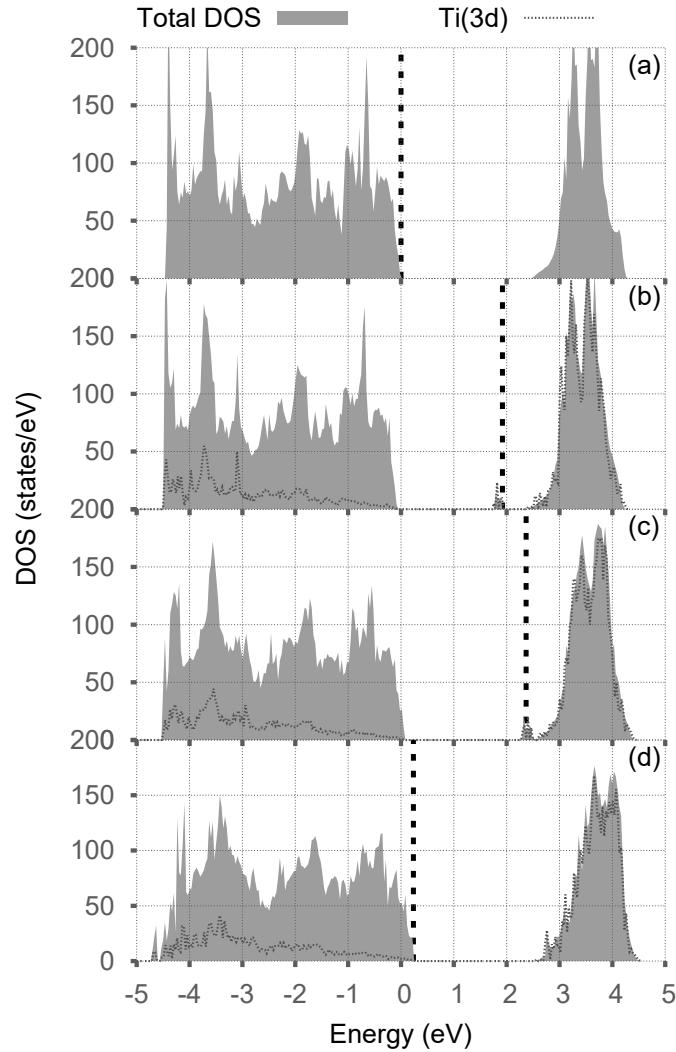


Figure 4.2: DOS of pure anatase (a) and anatase with  $V_O$ ,  $V_O^{+1}$  and  $V_O^{+2}$  (b)-(d) respectively with Ti 3d states also shown. Black dotted line represents the  $E_F$  and VBM of pure anatase has been chosen as the reference for all the plots.

### 4.3 Neutral and charged titanium interstitials ( $Ti_i$ , $Ti_i^{+1}$ , $Ti_i^{+2}$ , $Ti_i^{+3}$ , $Ti_i^{+4}$ )

A Ti atom has a valence state of four, hence introducing  $Ti_i$  in anatase leads to four unpaired electrons. DOS plot of anatase with  $Ti_i$  clearly showed the formation of mid-gap defect states. The gap states were found to be spread over a narrow energy range, indicating that the gap states were localized (see Fig. 4.3(b)). However,  $E_F$  was found to lie in the conduction band, suggesting that some of the excess charge carriers (or unpaired electrons of  $Ti_i$ ) got delocalized, while the rest could be localized and present in the gap state.

DOS plots of anatase with different charge states of Ti interstitial clearly showed that the mid-gap defect states were associated with Ti 3d orbitals (see Fig. 4.3(a)-(f)). For  $Ti_i^{+1}$ ,  $E_F$  was still found to be positioned in the conduction band, however, the distance between it and the CBE decreased as compared to that of  $Ti_i$  (i.e., 0.34 eV for  $Ti_i$  and 0.21 eV for  $Ti_i^{+1}$ ; see Fig. 4.3(b) and 4.3(c)). Further, in the case of  $Ti_i^{+2}$ ,  $E_F$  was found to be located at the edge of the mid gap state (see Fig. 4.3(d)), indicating the two electrons which were removed from  $Ti_i$  to create  $Ti_i^{+1}$  and  $Ti_i^{+2}$  successively being present in the conduction band, hence suggesting the presence of the two defect states in the conduction band because of  $Ti_i$ . Moreover, when one more electron was removed to create  $Ti_i^{+3}$ ,  $E_F$  shifted to the middle of the mid gap defect state and finally for  $Ti_i^{+4}$  it was found to coincide with the VBM (see Fig. 4.3(e)-(f)). These observations indicate that the two electrons which were removed to create  $Ti_i^{+3}$  and  $Ti_i^{+4}$  successively from  $Ti_i^{+2}$ , occupied the localized mid gap defect states. Thus,  $Ti_i$  was found to create two localized defect states in the band gap of anatase, whereas two delocalized states were formed in the conduction band. The presence of delocalized states in the conduction band and the possibility of excitation of electrons from the gap state to the conduction band, could introduce intrinsic  $n$ -type conductivity in anatase with  $Ti_i$ .

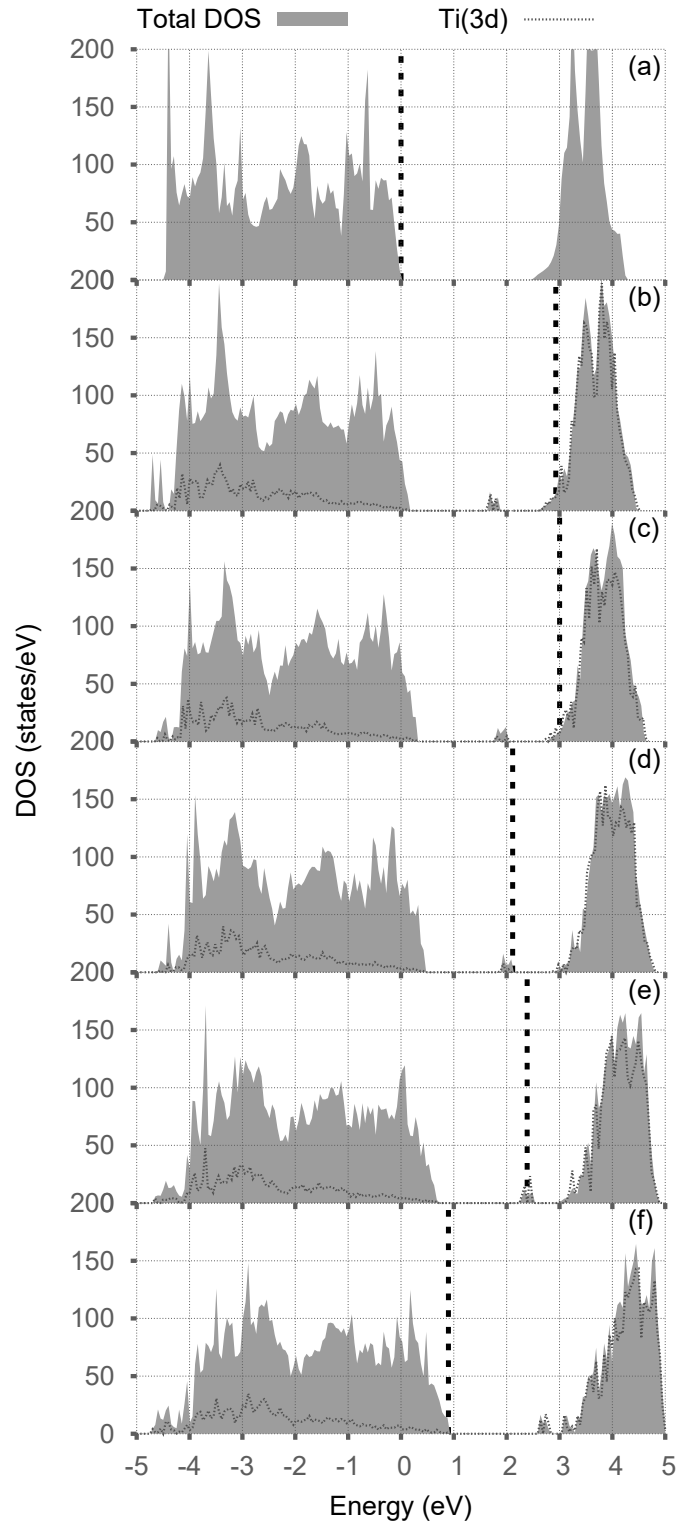


Figure 4.3: DOS of pure anatase (a) and anatase with  $Ti_i$ ,  $Ti_i^{+1}$ ,  $Ti_i^{+2}$ ,  $Ti_i^{+3}$  and  $Ti_i^{+4}$  (b)-(f) respectively with Ti 3d states also shown. Black dotted line represents the  $E_F$  and VBM of pure anatase has been chosen as the reference for all the plots.

## 4.4 Titanium vacancies ( $V_{Ti}$ ) and oxygen interstitials ( $O_i$ )

For these systems, no mid-gap defect states were found to form (see Fig. 4.4(a)-(d)). DOS plot for the defect associated O atoms (O atoms surrounding the defect sites) showed O 2*p* states being formed inside the valence band. These states were found to be spread over a wide energy range, indicating these as delocalized states (Fig. 4.4(c)-(d)).

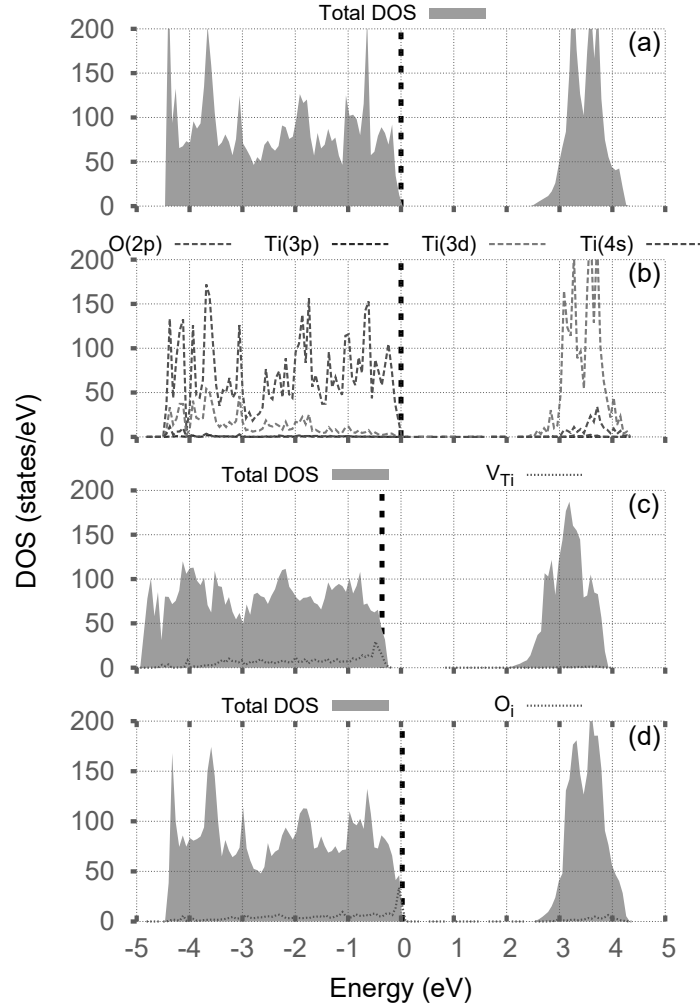


Figure 4.4: Total DOS (a) and PDOS (b) of anatase. DOS of anatase with  $V_{Ti}$ (c) and  $O_i$ (d). Red dotted line in (c) and (d) represents O 2*p* states (scaled by 5 times) due to the defect associated atoms. Black dotted line represents the  $E_F$  and VBM of pure anatase has been chosen as the reference for all the plots.



## 4.5 Stability of native defects: Formation energy analysis

The stability of various defect types under various conditions were compared using the formation energy analysis. Fig. 4.5(a) and (b) show the formation energies of native defects under O-poor and O-rich conditions respectively, obtained as a function of  $E_F$ .  $E_F$  here signifies the electron richness of the system. For example, if the system is doped  $n$ -type, the charge carrier (electron) concentration would increase. This would make the system more electron rich and  $E_F$  would move towards the CBM. The upper and lower limits of  $E_F$  here correspond to the CBM and VBM respectively. The charge transition levels (denoted by  $\varepsilon$ ) of various native defects are shown in Table 4.2. Note that, these transition levels are  $E_F$  values at which a defect could be stable in multiple charged states.

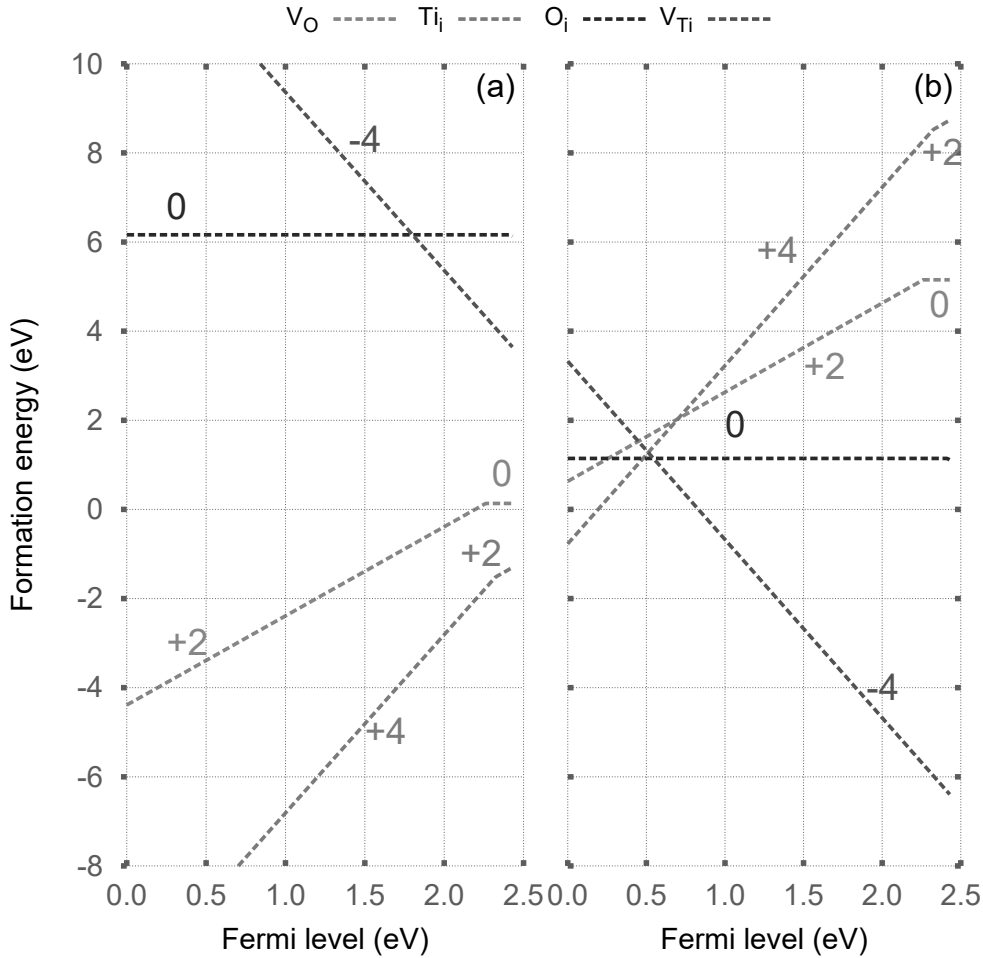


Figure 4.5: Defect formation energies of native defects as a function of Fermi level ( $E_F$ ) in O-poor (a) and O-rich (b) conditions. The lower and upper limits of fermi level correspond to VBM and CBM respectively.

For a wide range of  $E_F$  (from 0 to  $\approx 2.2$  eV), the most stable charged states of Ti vacancies, O vacancies and Ti interstitial were found to be -4, +2 and +4 respectively (see Fig. 4.5(a) and (b)), suggesting these native defects as quadruple acceptor, double donor, and quadruple donor respectively. The most stable charge state for O interstitials was found to be 0. In O-poor and in O-rich conditions, the most stable defect states (lowest formation energies) were found to be  $Ti_i^{+4}$  and  $V_{Ti}^{-4}$  respectively. Moreover, in O-poor condition,  $Ti_i^{+4}$  was found to be the most stable

Table 4.2: Charge transition levels (in eV) of various native defects with respect to the VBM

Defect	Charge states (q, q')	Transition level $\varepsilon(q, q')$
$V_O$	+2/+1	2.27
	+1/0	2.28
$Ti_i$	+4/+3	2.33
	+3/+2	2.34
	+2/+1	2.73
	+1/0	2.74
$V_{Ti}$	0/-1	0.01
	-1/-2	0.02
	-2/-3	0.03
	-3/-4	0.04
$O_i$	0/-1	2.42
	-1/-2	2.43

defect state for the entire range of  $E_F$ . O interstitials were found to have a positive formation energy for both the conditions considered and thus were unlikely to form spontaneously under equilibrium conditions. The stability of neutral state for O interstitial could also explain the binding of the interstitial O atom with a lattice oxygen atom and forming a dimer configuration (discussed in Section 4.1). Oxygen vacancies in the form of  $V_O^{+2}$  were found to have a negative formation energy (and hence stable) for  $E_F$  ranging between 0 and 2.2 eV in O-poor conditions and hence are likely to form.

The charge transition levels for O vacancies ( $\varepsilon(+2, +1)$  and  $\varepsilon(+1, 0)$ ) were found to lie only slightly below the CBM (0.16 eV; see Table 4.2) indicating these as shallow donor type defects. As a result, neutral O vacancy could ionize easily, and thereby lead to intrinsic  $n$ -type conductivity in anatase. Similarly, out of the four transition levels of  $Ti_i$ , two (i.e.,  $\varepsilon(+4, +3)$  and  $\varepsilon(+3, +2)$ ) were found to locate close to the CBM, whereas the other two (i.e.,  $\varepsilon(+2, +1)$  and  $\varepsilon(+1, 0)$ ) were positioned in the conduction band, thereby clearly indicating that Ti interstitial could also provide  $n$ -type conductivity to anatase. Note that, the transition levels of Ti vacancies (from  $\varepsilon(0, -1)$  to  $\varepsilon(-3, -4)$ ) were found to lie close to the valence band edge, indicating these as shallow acceptor type defects. Finally, the transition levels of O interstitials ( $\varepsilon(0, -1)$ ) and  $\varepsilon(-1, -2)$  were found to lie  $\approx 0.02$  eV below the CBM, but these would be very unlikely to form due to their high formation energy under both O-rich and O-poor conditions.

It is interesting to note that, in O-poor condition, donor type defects (O vacancy and Ti interstitial) were found to be more stable (lower formation energy) than the acceptor type defects (Ti vacancy and O interstitial). This could then lead to an incomplete compensation of the electrons (induced by the donor-type defects) by the holes (induced by the acceptor-type defects), thereby making anatase intrinsically  $n$ -type, reason behind the growth of intrinsically  $n$ -type anatase for oxygen deficient samples. However, in O-rich conditions, the acceptor-type defect states (mainly Ti vacancy) were found to have a lower formation energy, which could make anatase  $p$ -type under these conditions.

# Chapter 5

## Dopants

To simulate doped anatase, a single Ti atom in the 96 atoms  $\text{TiO}_2$  supercell was substituted with the dopant atom. This leads to a dopant concentration of 3.125 at%. Since all the Ti atoms in the supercell are equivalent, any atom can be substituted.

### 5.1 Niobium ( $\text{Nb}_{\text{Ti}}$ )

The lattice parameters and bond lengths of Nb-doped anatase are shown in Table 5.1. There was a larger increase in parameters  $a$  and  $b$  than in the lattice parameter  $c$ . Moreover, for the Nb-O bond, there was an increment along the apical direction, and a slight decrease along the equatorial direction. The increase in lattice parameters  $a$ ,  $b$  and  $c$  could be due to the larger atomic size of the  $\text{Nb}^{+5}$  ion than the  $\text{Ti}^{+4}$  ion that it substitutes. To accommodate the larger dopant atom, the supercell relaxes outward.

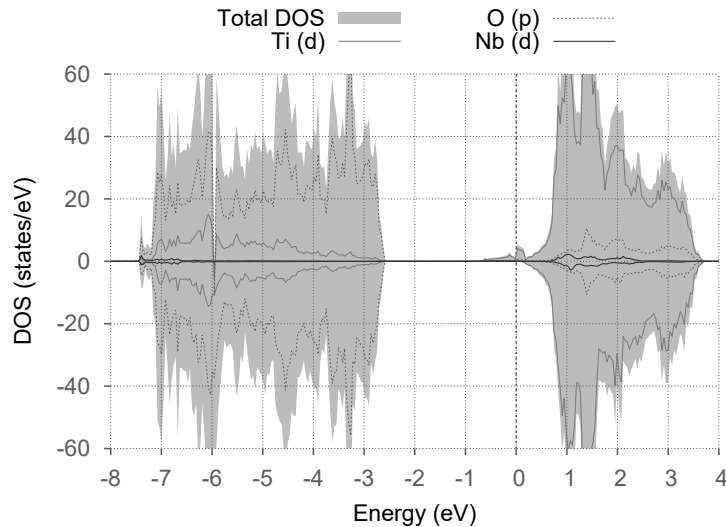


Figure 5.1: PDOS of Nb-doped anatase.  $E_F$  has been shifted to 0 eV

The PDOS plot for Nb-doped anatase is shown in Fig. 5.1 and the band structure is shown in Fig. 5.2. Ti  $d$  states dominate the conduction band and O  $p$  states dominate the valence band. The dopant states (Nb  $d$ ) were spread in the conduction band forming resonant states. Nb dopant did not form any mid gap states. A previous GGA+U study also concluded that Nb dopant does not form any mid gap states [29]. The Fermi level was positioned at the conduction

Table 5.1: Change in lattice parameters and bond lengths of Nb-doped anatase with respect to pristine anatase.  $\Delta_{bond}$  is the change in Nb-O bond length w.r.t. Ti-O bond length.

$\Delta a = \Delta b$	$\Delta c$	$\Delta_{bond}$	
		Apical	Equatorial
+0.17%	+0.07%	+1.73%	-0.74%

band edge. This means that the dopant Nb atom, donates extra electrons in the conduction band, imparting  $n$ -type conductivity. This could improve the conductivity of anatase. There was also a reduction in the band gap by 0.78 eV. This is slightly disadvantageous for TCO applications because a reduced band gap would mean reduced transparency. Improved conductivity in Nb doped anatase thin films has also been observed experimentally [17, 79].

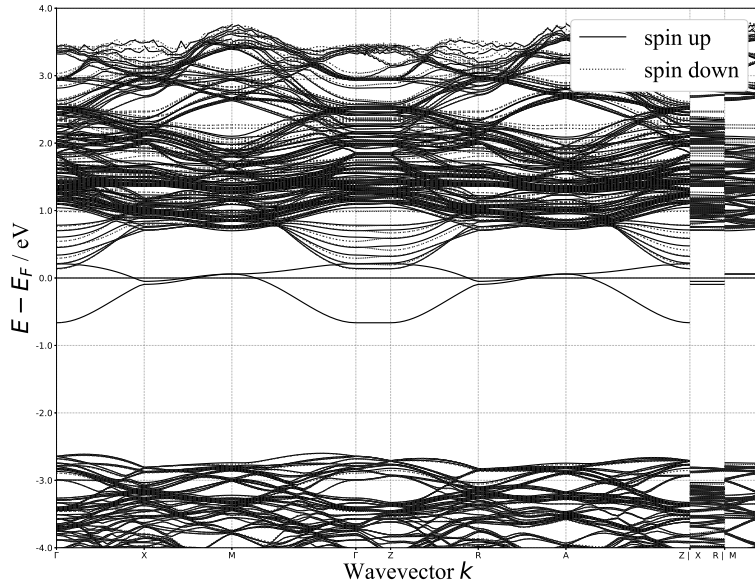


Figure 5.2: Band structure of Nb-doped anatase.  $E_F$  has been shifted to 0 eV

Bader charge analysis showed the charge on Nb atom to be +2.81. This positive charge is more than the charge on the Ti atom (+2.41) that it substitutes. This means that when an Nb atom displaces a Ti atom from the supercell, there is a negative charge transfer from this atomic site. Bader analysis further showed that this negative charge is distributed over the Ti atoms because the effective positive charge on Ti atoms reduced in the doped system.

## 5.2 Tantalum ( $Ta_{Ti}$ )

The lattice parameters and bond lengths of Ta-doped anatase are shown in Table 5.2. There was an increase in parameters  $a$  and  $b$  but the supercell shrunk slightly along  $c$ . Moreover, for the Ta-O bond, there was an increment along both the apical and equatorial directions. The increase

in Ta-O bond lengths could be due to the larger atomic size of the Ta<sup>+5</sup> ion than the Ti<sup>+4</sup> ion that it substitutes. To accommodate the larger dopant atom, the supercell relaxes outward.

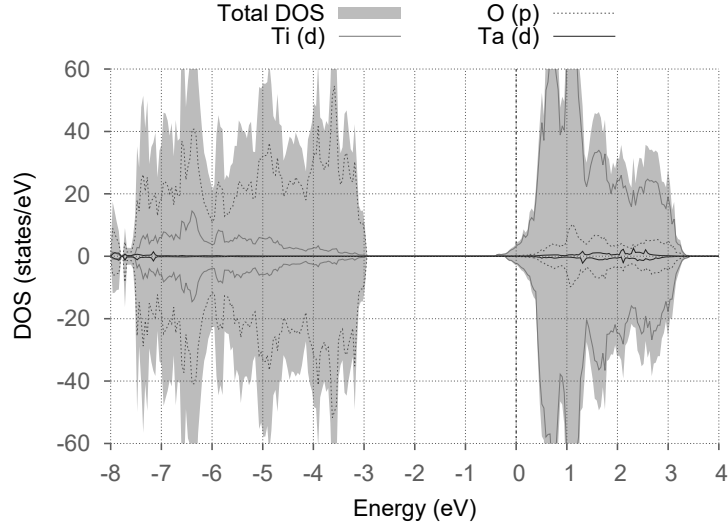


Figure 5.3: PDOS of Ta-doped anatase.  $E_F$  has been shifted to 0 eV

Table 5.2: Change in lattice parameters and bond lengths of Ta-doped anatase with respect to pristine anatase.  $\Delta_{bond}$  is the change in Ta-O bond length w.r.t. Ti-O bond length.

$\Delta a = \Delta b$	$\Delta c$	$\Delta_{bond}$	
		Apical	Equatorial
+0.24%	-0.08%	+0.92%	0.29%

The PDOS plot for Ta-doped anatase is shown in Fig. 5.3 and the band structure is shown in Fig. 5.4.

The dopant states (Ta  $d$ ) formed deep in the conduction band as resonant states. Ta dopant did not form any mid gap states. The Fermi level was positioned in the conduction band near the conduction band edge. This means that the dopant Ta atom, donates extra electrons in the conduction band, imparting  $n$ -type conductivity. This could improve the conductivity of anatase, giving it a metallic like nature. The band gap was unchanged unlike Nb. These results are in agreement with a previous GGA+U study [80]. Improved conductivity in Ta-doped anatase thin films has also been observed experimentally [79, 81].

Bader charge analysis showed the charge on Ta atom to be +3.08. This positive charge is more than the charge on the Ti atom (+2.41) that it substitutes. This means that when a Ta atom displaces a Ti atom from the supercell, there is a negative charge transfer from this atomic site. Ta-doped anatase would exhibit good optoelectronic properties because of the Fermi level crossing the conduction band (hence, improved conductivity) and transparency originating from the band gap of the host anatase material.

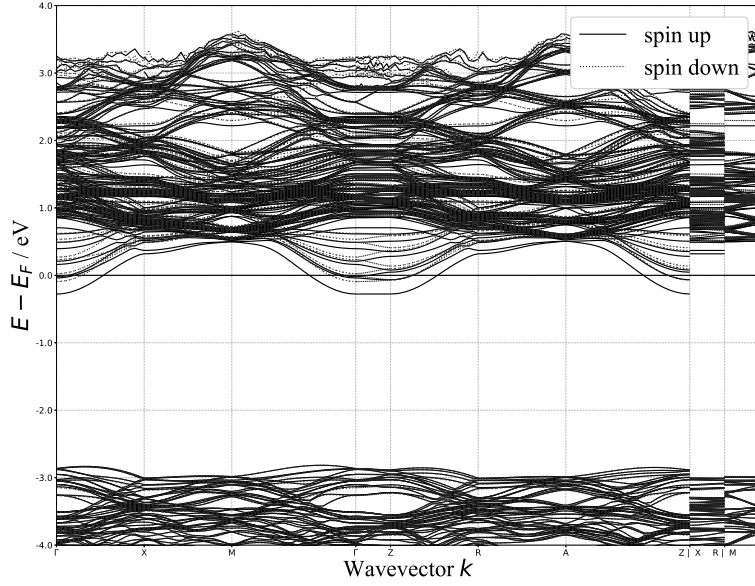


Figure 5.4: Band structure of Ta-doped anatase.  $E_F$  has been shifted to 0 eV

### 5.3 Vanadium ( $V_{Ti}$ )

The lattice parameters and bond lengths of V-doped anatase are shown in Table 5.3. There was a slight increase in parameters  $a$  and  $b$  but the supercell shrunk along  $c$ . The shrinkage along  $c$  direction could be attributed to the significant decrease in the apical V-O bond length, so much so that it became smaller than the equatorial V-O bond.

Table 5.3: Change in lattice parameters and bond lengths of V-doped anatase with respect to pristine anatase.  $\Delta_{bond}$  is the change in V-O bond length w.r.t. Ti-O bond length.

$\Delta a = \Delta b$	$\Delta c$	$\Delta_{bond}$	
		Apical	Equatorial
+0.11%	-0.32%	-3.40%	+0.65%

The PDOS plot for V-doped anatase is shown in Fig. 5.5 and the band structure is shown in Fig. 5.6. The dopant states (V  $d$ ) were formed both as localized states near the conduction band edge and as delocalized states deep in the conduction band. V dopant did not form any mid gap states. The Fermi level was positioned at the valence band edge. There was no significant change in the band gap.

Bader charge analysis showed the charge on V atom to be +2.32. This positive charge is slightly smaller than the charge on the Ti atom (+2.41) that it substitutes. This means that when a V atom displaces a Ti atom from the supercell, there is a negative charge transfer towards this atomic V site. With Fermi level lying at the valence band edge, V doped anatase does not attain improved  $n$ -type conductivity like Nb and Ta.

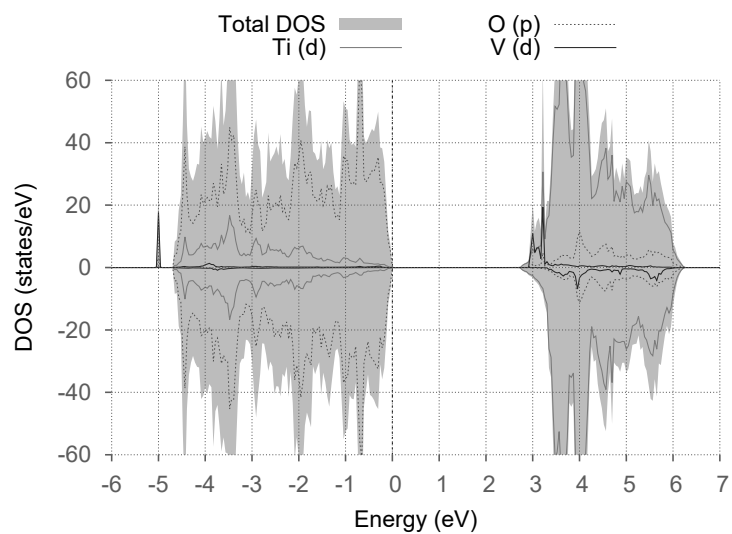


Figure 5.5: PDOS of V-doped anatase.  $E_F$  has been shifted to 0 eV

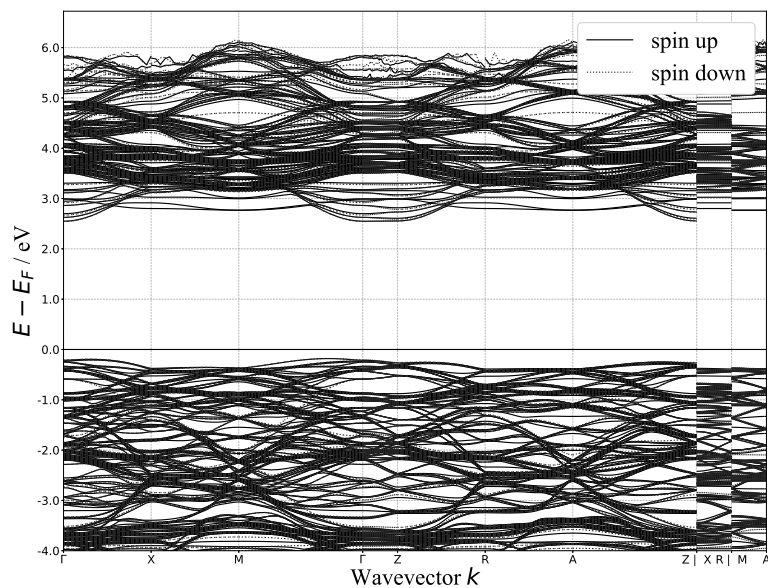


Figure 5.6: Band structure of V-doped anatase.  $E_F$  has been shifted to 0 eV

## 5.4 Molybdenum ( $Mo_{Ti}$ )

The lattice parameters and bond lengths of Mo-doped anatase are shown in Table 5.4. There was a slight increase in parameters  $a$  and  $b$  but the supercell shrunk along  $c$ . Both the apical and equatorial Mo-O bond lengths got increased.

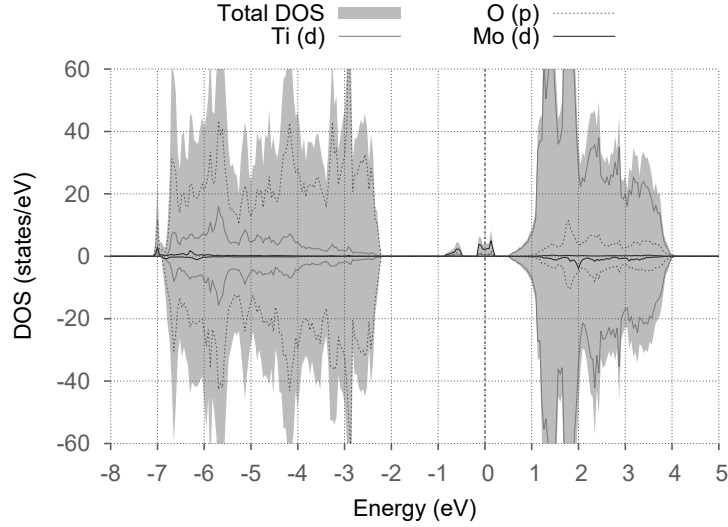


Figure 5.7: PDOS of Mo-doped anatase.  $E_F$  has been shifted to 0 eV

Table 5.4: Change in lattice parameters and bond lengths of Mo-doped anatase with respect to pristine anatase

$\Delta a = \Delta b$	$\Delta c$	$\Delta_{bond}$	
		Apical	Equatorial
+0.18%	-0.09%	1.14%	2.00%

The PDOS plot for Mo-doped anatase is shown in Fig. 5.7 and the band structure is shown in Fig. 5.8. The dopant states (Mo  $d$ ) were formed both as localized mid-gap states and as delocalized states deep in the conduction band. Khan *et al.* also observed localized Mo  $d$  states, however the states in their calculations were more closer to the conduction band than in the current work [82]. This could probably be due to the different  $U$  values used in the two studies. The Fermi level was positioned inside mid-gap states, which means that some of the mid-gap states are occupied. The charge density plot (Fig. 5.9) for the mid-gap state further shows that, the mid-gap state arises mainly from localized electrons on the dopant Mo atom and nearby O atoms.

Bader charge analysis showed the charge on Mo atom to be +2.4. This positive charge is equal to the charge on the Ti atom (+2.41) that it substitutes. Due to electron transitions from valence band to mid-gap states and from mid-gap states to conduction band, Mo-doped anatase can absorb additional wavelengths of light, hence transparency could get reduced.



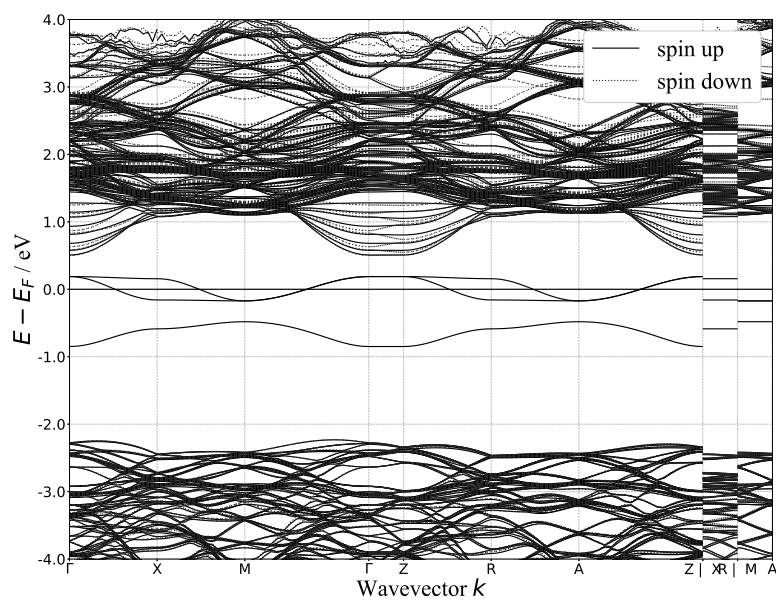


Figure 5.8: Band structure of Mo-doped anatase.  $E_F$  has been shifted to 0 eV

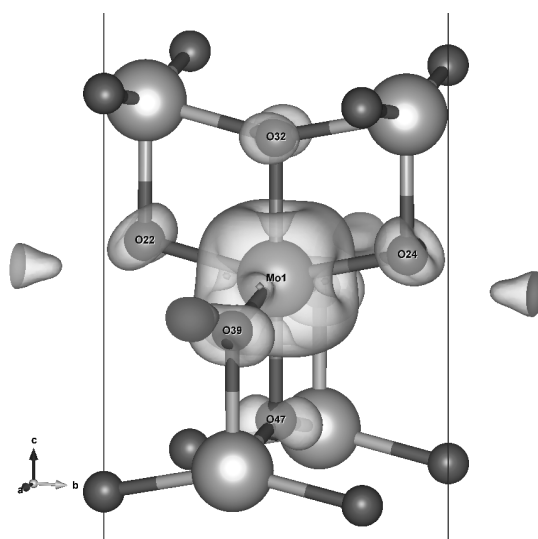


Figure 5.9: Charge density isosurface for Mo-doped anatase plotted in the region of mid-gap state

## 5.5 Tungsten ( $W_{Ti}$ )

The lattice parameters and bond lengths of W-doped anatase are shown in Table 5.5. There was an increase in parameters  $a$  and  $b$  but the supercell shrunk along  $c$ . Both the apical and equatorial W-O bond lengths increased.

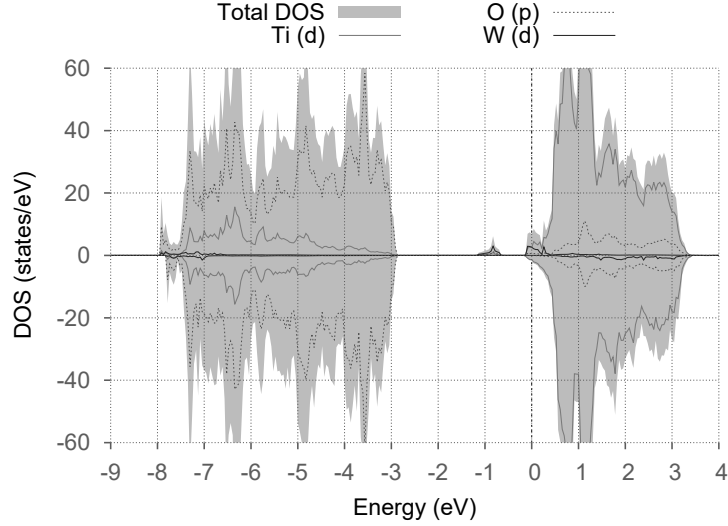


Figure 5.10: PDOS of W-doped anatase.  $E_F$  has been shifted to 0 eV

Table 5.5: Change in lattice parameters and bond lengths of W-doped anatase with respect to pristine anatase

$\Delta a = \Delta b$	$\Delta c$	$\Delta_{bond}$	
		Apical	Equatorial
+0.21%	-0.10%	0.39%	2.32%

The PDOS plot for W-doped anatase is shown in Fig. 5.10 and the band structure is shown in Fig. 5.11. The dopant states (W  $d$ ) were formed both as localized mid-gap states and as states deep in the conduction band.

The Fermi level was positioned near the conduction band edge, which could mean W-doped anatase system to show increased  $n$ -type conductivity. The charge density plot (Fig. 5.12) for the mid-gap state further showed that, the mid-gap state arises mainly from localized electrons on the dopant W atom ( $d_{xy}$ ), four nearby O ( $p$ ) and Ti atoms. All these atoms lie in or close to the horizontal plane containing the dopant W atom.

Bader charge analysis showed the charge on W atom to be +2.73. This positive charge is higher than the charge on the Ti atom (+2.41) that it substitutes. This means that there is a net negative charge transfer from the dopant atom. This charge is then localized on the nearby Ti and O atoms in the horizontal plane of dopant atom. Due to electron transitions from valence band to mid-gap states and from mid-gap states to conduction band, W-doped anatase can absorb additional wavelengths of light, hence transparency is reduced. A previous experimental and computational (based on GGA) study, investigated W-doped anatase for optoelectronic applications [7]. The authors found W to form states in the conduction band with the Fermi level

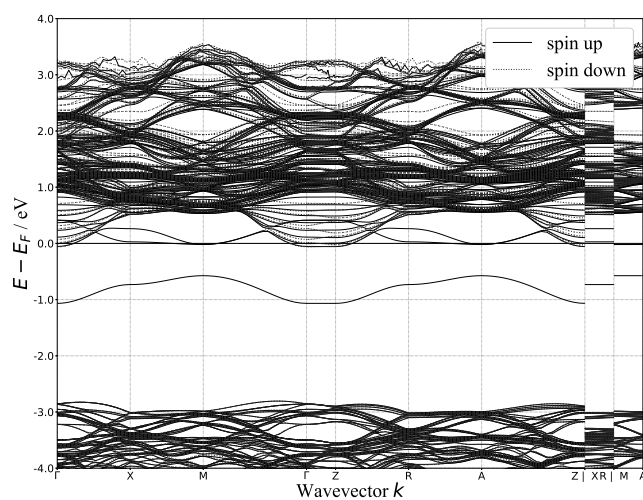


Figure 5.11: Band structure of W-doped anatase.  $E_F$  has been shifted to 0 eV

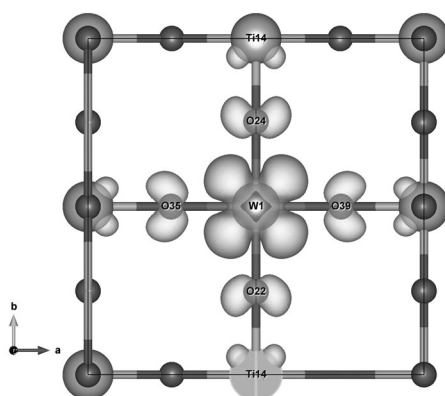


Figure 5.12: Charge density isosurface for W-doped anatase plotted on a 2d surface (containing W dopant atom) in the region of mid-gap state

lying in the conduction band. This is consistent with the current work. However, unlike in the current work, they did not find any mid gap state. This discrepancy could be due to GGA trying to delocalize the electrons in the previous study.

## 5.6 Chromium ( $Cr_{Ti}$ )

The lattice parameters and bond lengths of Cr-doped anatase are shown in Table 5.6. The entire supercell shrunk and the amount of shrinkage was higher along  $c$ . Both the apical and equatorial Cr-O bond lengths were reduced. The lattice shrinkage could be due to the smaller atomic size of Cr than Ti.

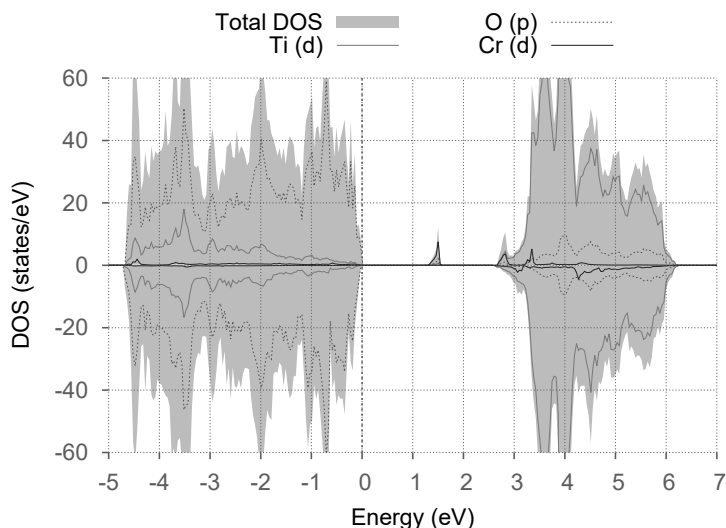


Figure 5.13: PDOS of Cr-doped anatase.  $E_F$  has been shifted to 0 eV

Table 5.6: Change in lattice parameters and bond lengths of Cr-doped anatase with respect to pristine anatase

$\Delta a = \Delta b$	$\Delta c$	$\Delta_{bond}$	
		Apical	Equatorial
-0.07%	-0.26%	-1.57%	-2.63%

The PDOS plot for Cr-doped anatase is shown in Fig. 5.13 and the band structure is shown in Fig. 5.14. The dopant states (Cr  $d$ ) were prominently formed as localized mid-gap states.

The Fermi level was positioned at the valence band edge. The charge density plot (Fig. 5.12) for the mid-gap state further showed that, the mid-gap state arises mainly from localized electrons on the dopant Cr atom ( $d_{xy}$  orbital) and four nearby O ( $p$ ) atoms. All these atoms lie in or close to the horizontal plane containing the dopant Cr atom.

Bader charge analysis showed the charge on Cr atom to be +2.13. This positive charge is lower than the charge on the Ti atom (+2.41) that it substitutes. This means that there is a net negative charge transfer towards the dopant atom site from the neighbouring atoms. Due to electron transitions from valence band to mid-gap states and from mid-gap states to conduction band, Cr-doped anatase can absorb additional wavelengths of light, hence transparency could become reduced. It would not show increased  $n$ -type conductivity like Nb- and Ta-doped systems, because the Fermi level is still pinned at the valence band edge.

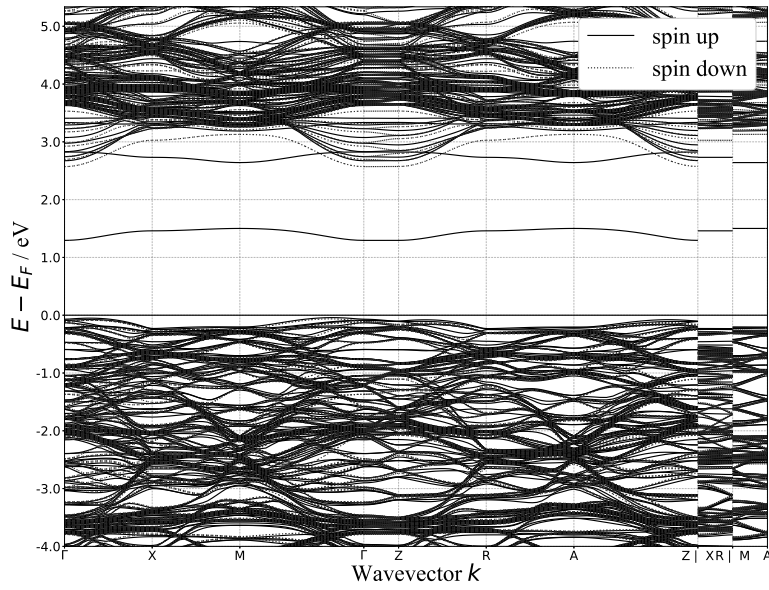


Figure 5.14: Band structure of Cr-doped anatase.  $E_F$  has been shifted to 0 eV

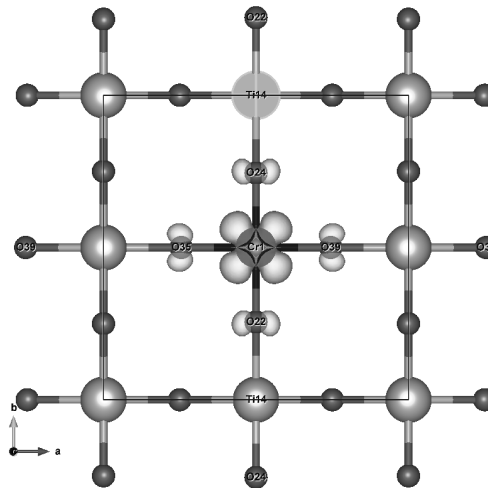


Figure 5.15: Charge density isosurface for Cr-doped anatase plotted on a horizontal layer (containing Cr dopant atom) in the region of mid-gap state

## 5.7 Lanthanum ( $La_{Ti}$ )

The lattice parameters and bond lengths of La-doped anatase are shown in Table 5.7. The entire supercell expanded and the amount of expansion was significant along  $c$  direction. Both the apical and equatorial La-O bond lengths increased significantly. The large atomic radius of La atom could be the reason for the observed lattice expansion.

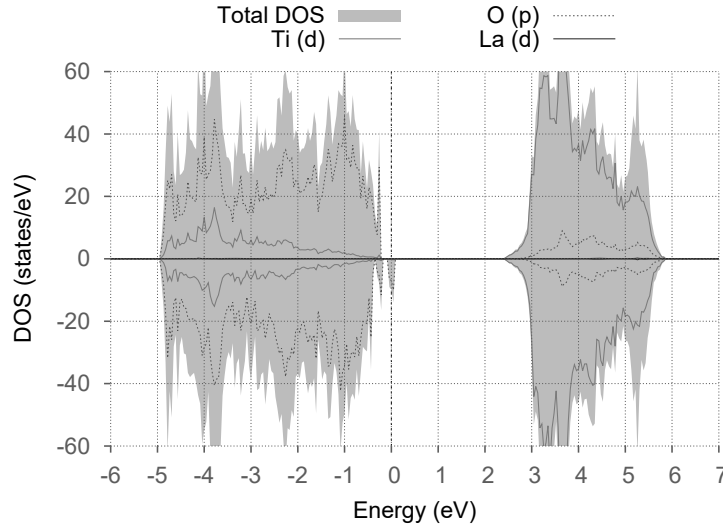


Figure 5.16: PDOS of La-doped anatase.  $E_F$  has been shifted to 0 eV

Table 5.7: Change in lattice parameters and bond lengths of La-doped anatase with respect to pristine anatase

$\Delta a = \Delta b$	$\Delta c$	$\Delta_{bond}$	
		Apical	Equatorial
+0.10%	+2.25%	+17.58%	+19.00%

The PDOS plot for La-doped anatase is shown in Fig. 5.16 and the band structure is shown in Fig. 5.17. The dopant states (La  $d$ ) did not form any mid-gap states. However, states were formed near the valence band edge. These states were associated with electrons in O  $p$  orbitals, as shown in Fig. 5.18. Due to states forming at the valence band edge, the band gap got reduced by 0.38 eV. The Fermi level was positioned near the valence band edge. These results agree with previous computational reports using DFT+ $U$  [83].

Bader charge analysis showed the charge on La atom to be +2.24. This positive charge is lower than the charge on the Ti atom (+2.41) that it substitutes. This means that there is a net negative charge transfer towards the dopant atom site from the neighbouring atoms. Due to reduction of the band gap, La-doped anatase can absorb higher wavelengths of light (red shift), hence transparency is reduced. It would not show increased  $n$ -type conductivity like Nb- and Ta-doped systems, because the Fermi level is still pinned near the valence band edge.

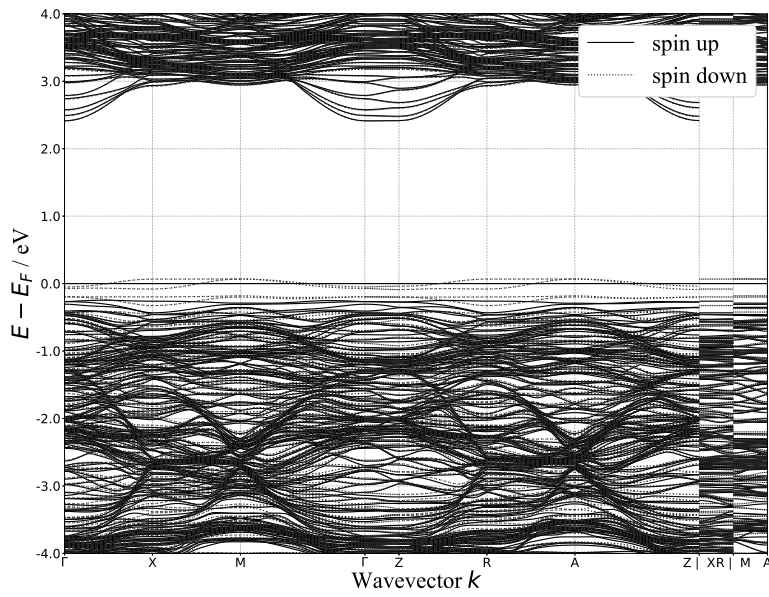


Figure 5.17: Band structure of La-doped anatase.  $E_F$  has been shifted to 0 eV

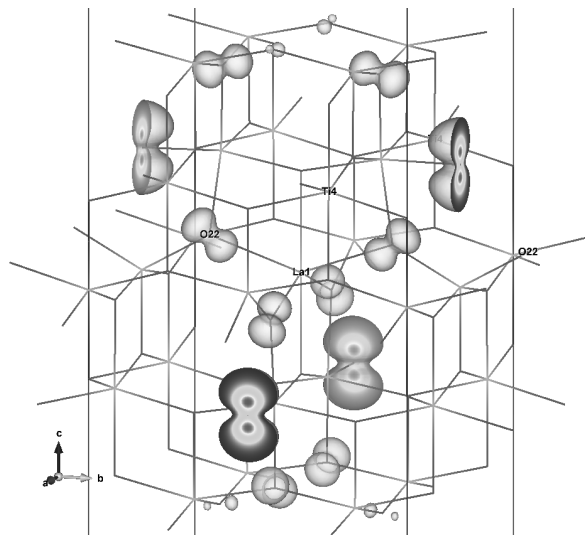


Figure 5.18: Charge density isosurface for La-doped anatase plotted in the region of localized states formed near the valence band edge

## 5.8 Copper ( $Cu_{Ti}$ )

The lattice parameters and bond lengths of Cu-doped anatase are shown in Table 5.8. The supercell expanded slightly along  $a$  and  $b$  directions. There was a shrinkage along  $c$  direction. Both the apical and equatorial Cu-O bond lengths were found to increase.

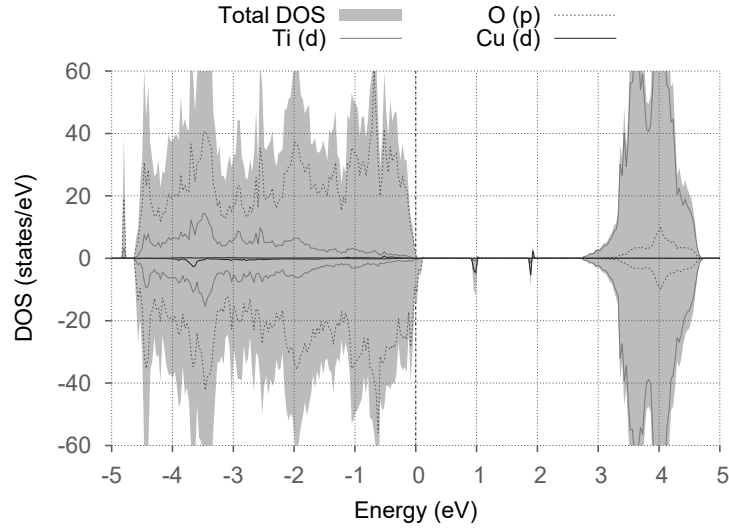


Figure 5.19: PDOS of Cu-doped anatase.  $E_F$  has been shifted to 0 eV

Table 5.8: Change in lattice parameters and bond lengths of Cu-doped anatase with respect to pristine anatase

$\Delta a = \Delta b$	$\Delta c$	$\Delta_{bond}$	
		Apical	Equatorial
+0.09%	-0.41%	+0.58%	+0.26%

The PDOS plot for Cu-doped anatase is shown in Fig. 5.19 and the band structure is shown in Fig. 5.20.

The mid-gap states were formed at two locations in the band gap: one closer to the VBM and the other closer to the CBM. The ones closer to the valence band edge were associated with Cu  $d_{z^2}$  and O  $p$  states (on O atoms bonded to the Cu atom) (see Fig. 5.21(a)). The mid-gap state closer to the conduction band edge was composed of Cu  $d_{x^2-y^2}$  and O  $p$  orbitals on O atoms near the Cu atom (see Fig. 5.21(b)). The Fermi level was positioned in the valence band near the valence band edge.

Bader charge analysis showed the charge on Cu atom to be +1.45. This positive charge is lower than the charge on the Ti atom (+2.41) that it substitutes. This means that there is a net negative charge transfer towards the dopant atom site from the neighbouring atoms. Due to electron transitions from valence band to mid-gap states and from mid-gap states to conduction band, Cu-doped anatase can absorb additional wavelengths of light, hence transparency would be reduced. It would not show increased  $n$ -type conductivity, because the Fermi level is still pinned near the valence band edge.



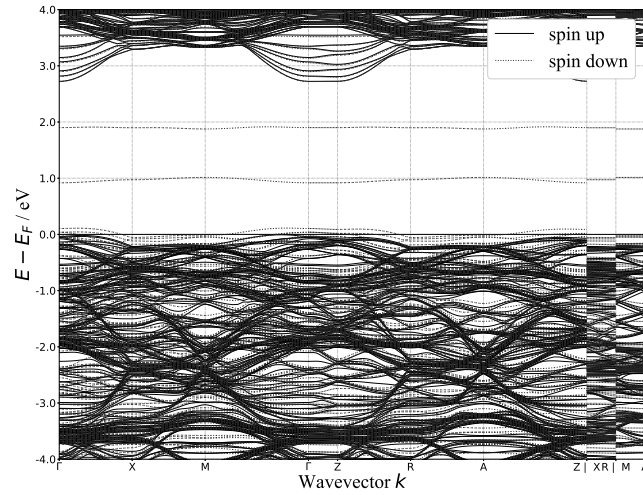


Figure 5.20: Band structure of Cu-doped anatase.  $E_F$  has been shifted to 0 eV

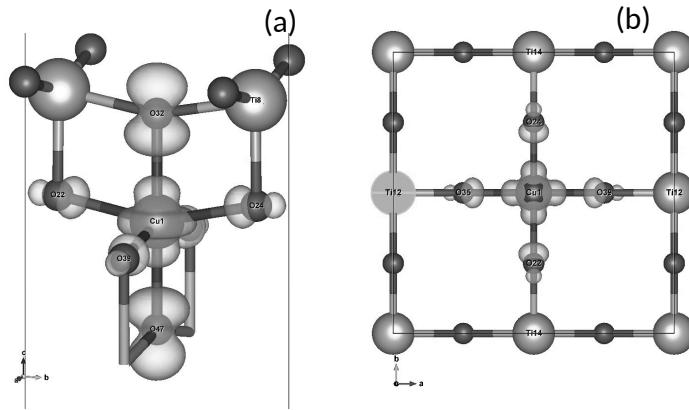


Figure 5.21: Charge density isosurface for Cu-doped anatase plotted in the region of localized states formed near the valence band edge (a) and near the conduction band edge (b)

## 5.9 Cobalt ( $CoTi$ )

The lattice parameters and bond lengths of Co-doped anatase are shown in Table 5.9. The supercell got shrunk along all the lattice directions. The maximum shrinkage was along  $c$  direction. Both the apical and equatorial Co-O bond lengths got reduced.

The PDOS plot for Co-doped anatase is shown in Fig. 5.22 and the band structure is shown in Fig. 5.23. The mid-gap states were formed at two locations in the band gap: one closer to the VBM and the other closer to the CBM. The ones closer to the valence band edge were found to be associated with Co  $d_{xy}$  and O  $p$  states (on O atoms bonded to the Co atom) (see Fig. 5.24(a)). The mid-gap state closer to the conduction band edge got localized on the dopant Co atom and nearby O atoms (see Fig. 5.24(b)). The Fermi level was at the valence band edge. The supercell was found to have a total magnetic moment of 5 Bohr magneton, majority of which came from the dopant Co atom.

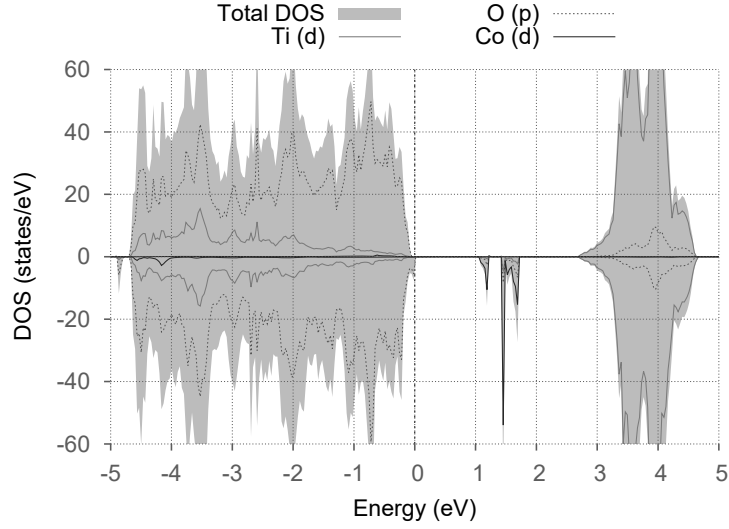


Figure 5.22: PDOS of Co-doped anatase.  $E_F$  has been shifted to 0 eV

Table 5.9: Change in lattice parameters and bond lengths of Co-doped anatase with respect to pristine anatase.  $\Delta_{bond}$  is the change in Co-O bond length w.r.t. Ti-O bond length.

$\Delta a = \Delta b$	$\Delta c$	$\Delta_{bond}$	
		Apical	Equatorial
-0.05%	-0.33%	-3.73%	-1.84%

Bader charge analysis showed the charge on Co atom to be +1.88. This positive charge is lower than the charge on the Ti atom (+2.41) that it substitutes. This means that there is a net negative charge transfer towards the dopant atom site from the neighbouring atoms. Due to electron transitions to/from mid-gap states, transparency would be reduced.

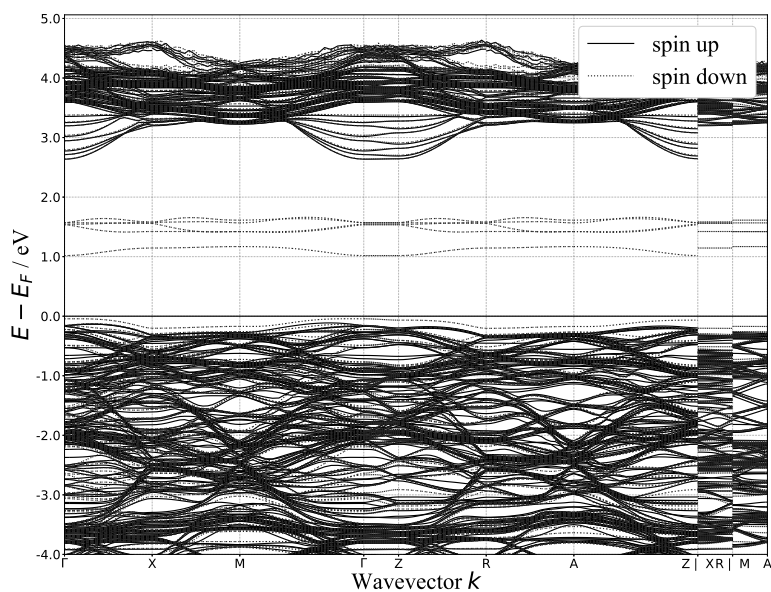


Figure 5.23: Band structure of Co-doped anatase.  $E_F$  has been shifted to 0 eV

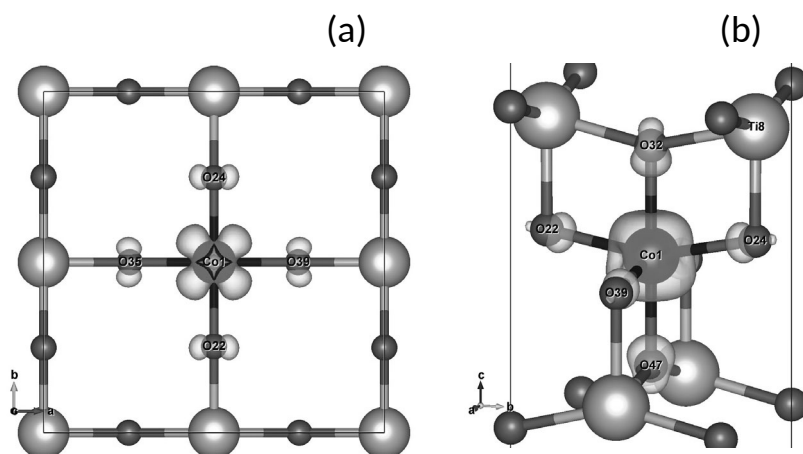


Figure 5.24: Charge density isosurface for a horizontal layer containing Co atom plotted in the region of localized states formed near the valence band edge (a) and near the conduction band edge (b)

## 5.10 Cerium ( $Ce_{Ti}$ )

The lattice parameters and bond lengths of Ce-doped anatase are shown in Table 5.10. The entire supercell expanded to accommodate the large Ce dopant atom. The maximum expansion was found to be along  $c$  direction. Both the apical and equatorial Ce-O bond increased significantly.

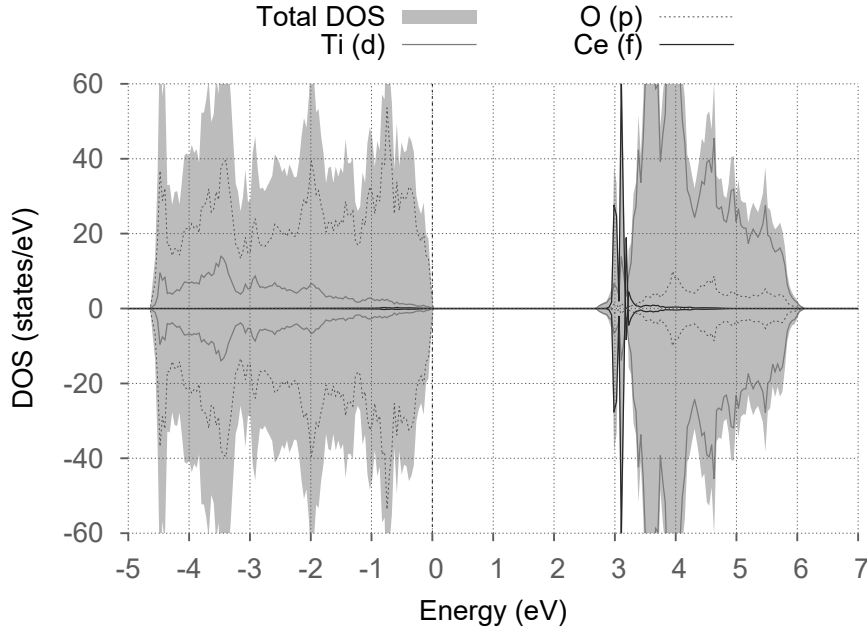


Figure 5.25: PDOS of Ce-doped anatase.  $E_F$  has been shifted to 0 eV

Table 5.10: Change in lattice parameters and bond lengths of Ce-doped anatase with respect to pristine anatase.  $\Delta_{bond}$  is the relative change in the Ce-O bond length w.r.t Ti-O bond length

$\Delta a = \Delta b$	$\Delta c$	$\Delta_{bond}$	
		Apical	Equatorial
+0.40%	+0.71%	+13.56%	+9.27%

The PDOS plot for Ce-doped anatase is shown in Fig. 5.25 and the band structure is shown in Fig. 5.26. The states due to the dopant Ce atom formed close to the conduction band edge inside the conduction band. These states were found to be localized on the  $f$  orbitals of Ce atom. The Fermi level was located at the valence band edge. These findings are consistent with other DFT+ $U$  reports [30].

Bader charge analysis showed the charge on Ce atom to be +2.55. This positive charge is lower than the charge on the Ti atom (+2.41) that it substitutes. This means that there is a net negative charge transfer towards the dopant atom site from the neighbouring atoms. There was a slight decrease ( $\approx 0.04$  eV) in the band gap.

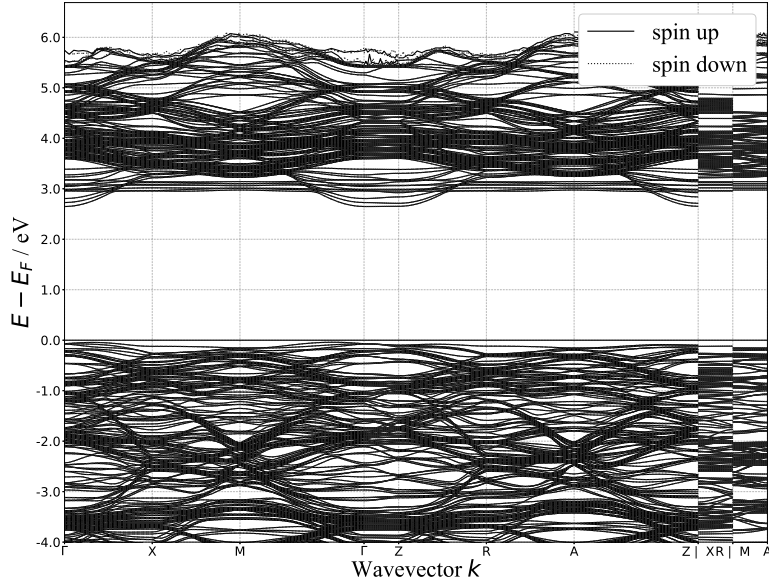


Figure 5.26: Band structure of Ce-doped anatase.  $E_F$  has been shifted to 0 eV

## 5.11 Effective mass analysis

Effective masses of charge carriers were calculated according to the schemes outlined in Chapter 2.

### 5.11.1 Pristine anatase

The finite difference effective masses of electrons at the conduction band edge along the  $\Gamma - X$  and the  $\Gamma - Z$  directions in the reciprocal space were found to be 0.54 and 5.10 respectively. Thus, there is a large anisotropy in the effective masses (and perhaps the mobility) of electrons. This is consistent with previous experimental and computational results [32, 58, 84]. Electrons were found to have an almost 10 times higher effective mass along  $\Gamma - Z$  direction as compared to  $\Gamma - X$  direction. The means that the bands are much flatter along  $\Gamma - Z$  direction than the  $\Gamma - X$  direction. The anisotropy becomes quite important, when anatase films are fabricated for optoelectronic applications, because the anisotropy could manifest as different electronic conductivities along different directions in anatase films. The finite difference effective mass of holes at the valence band edge along  $\Gamma - X$  direction was calculated to be 1.74 which is more than 3 times higher than that of electrons at the conduction band edge. This could mean that holes along valence band edge are less mobile than electrons at the conduction band edge. This also shows that doping anatase  $p$ -type with acceptor defects might not be very beneficial in increasing conductivity because of the higher effective mass (and low mobility) of holes in the valence band. Effective masses for electrons and holes in pristine anatase along the  $\Gamma - X$  direction are listed in Table. 5.11.

Fig. 5.27(a) and 5.27(b) show the fitting of DFT band dispersion for the conduction and valence band respectively.  $\alpha$  quantifies the non-parabolicity of the bands. All the computed values for electron effective mass yield almost equal values and the absolute value of  $\alpha$  is quite

Table 5.11: Charge carrier effective masses (along  $\Gamma - X$  direction) in pristine anatase

	Effective masses (in terms of $m_e$ )			$\alpha$
	Finite diff.	Least sq.	Kane mass	
Electron	0.54	0.54	0.54	0.44
Hole	1.74	1.64	1.79	-2.21

low. The optical effective mass for electron was computed to be 0.55, which is again almost equal to the finite difference effective mass. This means that the conduction band considered here is highly parabolic. For hole electron masses, however the values vary and the absolute value of  $\alpha$  is higher. Hence, non-parabolic nature is more in the case of conduction band edge than the valence band edge.

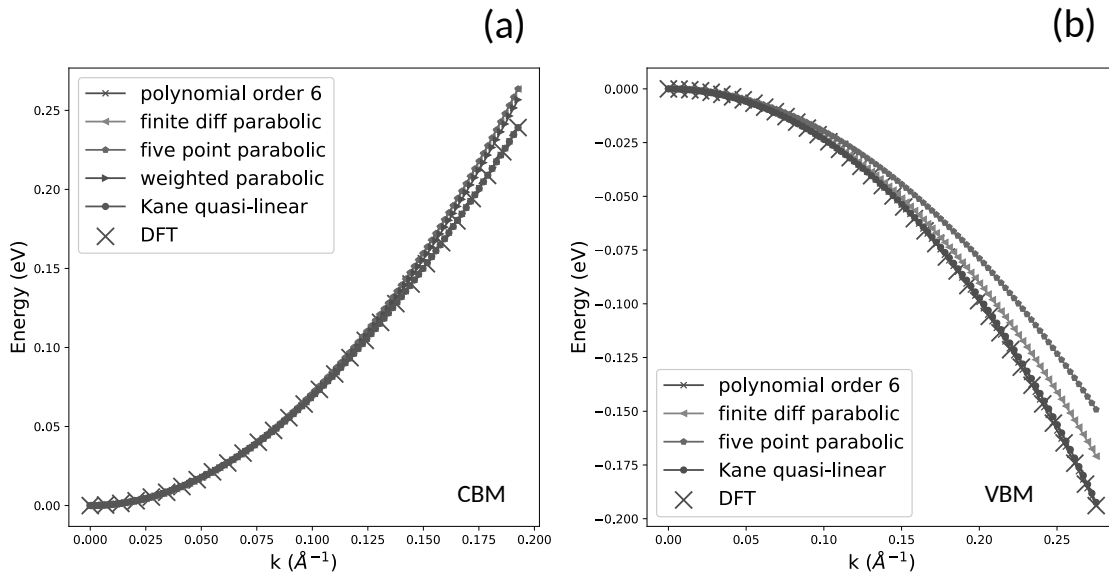


Figure 5.27: Band dispersion fitting at the conduction band edge (a) and valence band edge (b), along  $\Gamma - X$  direction

### 5.11.2 Dopants

Fig. 5.28(a) depicts the computed effective mass values for various doped systems and Fig. 5.28(b) shows the corresponding non-parabolicity parameter  $\alpha$ . The band dispersion was found to become more non-parabolic when dopants were introduced ( $\alpha$  for all the doped systems was found to be higher than pristine  $\text{TiO}_2$ ). The computed effective mass values (using various definitions) for Nb-, Ta-, W-, and Cr-doped anatase were more separated from each other than the other dopants. The disagreement was maximum in the case of Nb dopant. Interestingly, the non-parabolicity ( $\alpha$ ) parameter for these dopants was also higher as compared to the other dopants. Nb had the maximum value of  $\alpha$ . This shows that, these four systems have more non-

parabolicity in bands (at conduction band edge) than the other systems. The non-parabolicity of Nb- and Ta-doped anatase can also be seen when fitting of the band dispersion is attempted (see Fig. 5.29). The various fitting polynomials clearly deviate from each other (more in the case of Nb dopant). For non-parabolic bands, optical effective mass gives a better description because it takes into account the non-parabolicity (as discussed in section 2.13.4). If optical effective masses are compared, we can see that the effective masses of all the doped systems increased with respect to pristine anatase. This increment was more in the case of dopants Nb, Ta and W meaning that these dopant atoms perturb the conduction band edge more than the other dopants. The values of effective masses for Nb-doped anatase computed in this work agreed with previous literature reports [58]. Literature reports discussing effective masses of other doped systems are rare.

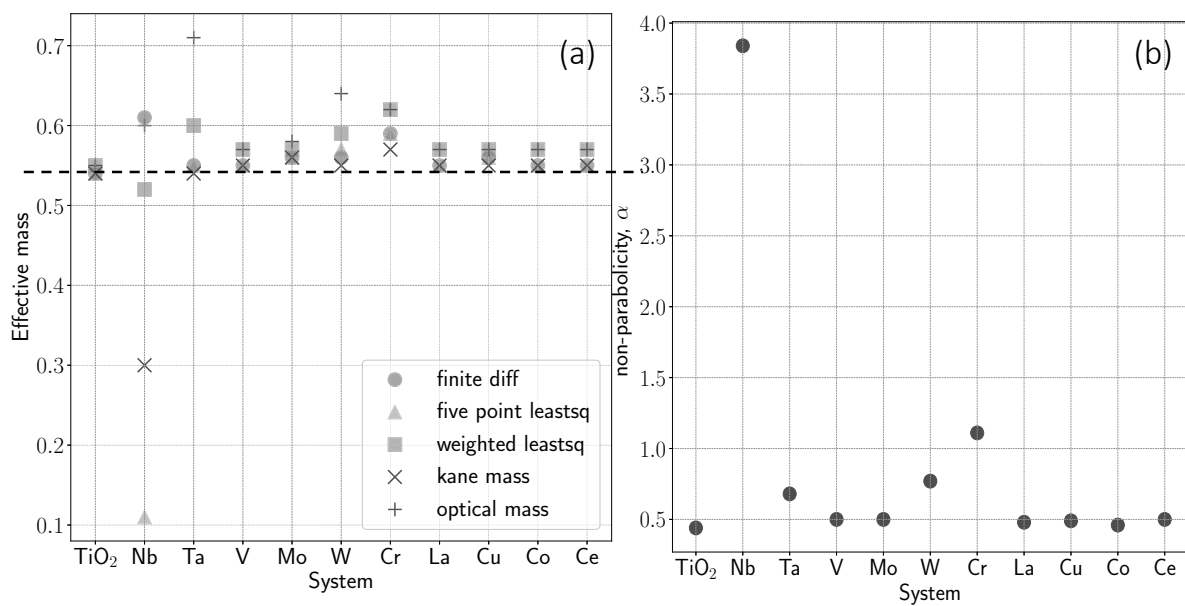


Figure 5.28: (a) Computed effective masses (as multiples of electron rest mass) of electrons for various doped systems and (b) corresponding  $\alpha$  values

Effective mass for the mid-gap states was also computed for a few cases (see Fig. 5.30). All mid-gap states had significantly higher effective masses than the effective mass of pristine anatase at the conduction band edge. This means that the bands are quite flat in nature and flatter bands mean more non-parabolic nature. That's why  $\alpha$  for all the mid-gap states is significantly higher than pristine anatase. If optical effective masses are compared for the mid-gap states, Cu-doped anatase has the highest effective mass. The flat nature of these bands and higher effective masses means that electrons in mid-gap states have quite low mobility and are localized (or trapped).

Effective masses were also computed for holes at the valence band edge (see Fig. 5.31 (a)). The effective mass for doped cases were slightly higher than that of pristine anatase with the exception on La, where the effective mass slightly decreased. The maximum increase in effective mass was seen in the case of Co-doped anatase, thus Co dopant causes the maximum perturbation of the valence band among all the dopants considered. It also had the most non-parabolic bands and highest value of  $\alpha$  among all the dopants. The non-parabolic nature of bands led

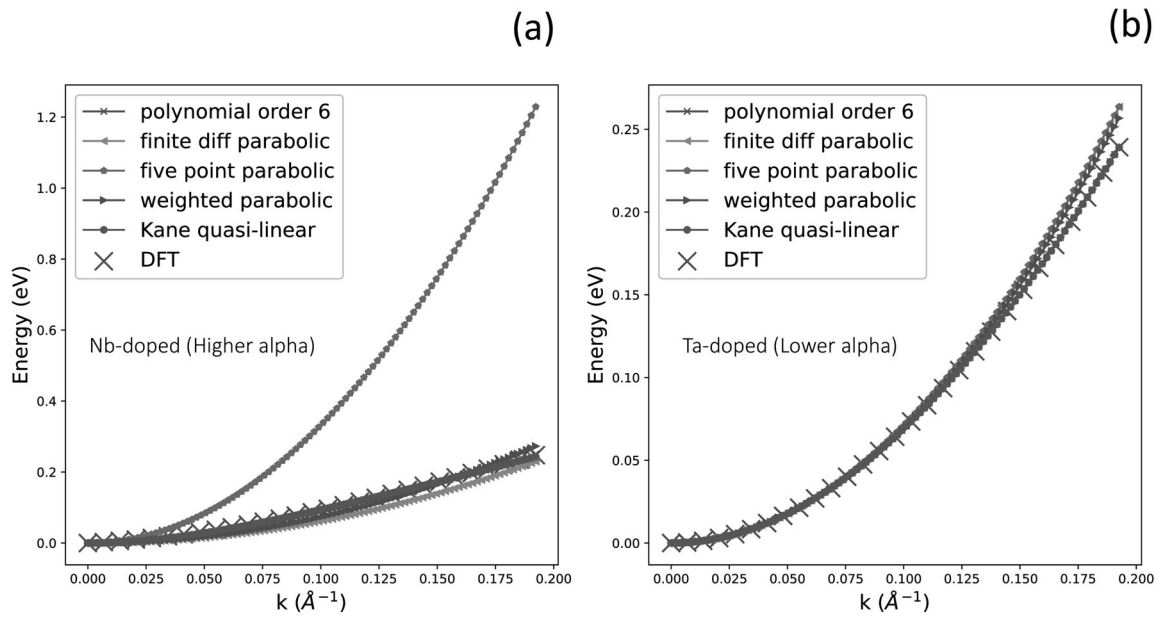


Figure 5.29: Band dispersion fitting at the conduction band edge along  $\Gamma - X$  direction for (a) Nb-doped anatase and (b) Ta-doped anatase

to the disagreements in effective masses computed using different algebraic definitions (see Fig. 5.31 (b)).



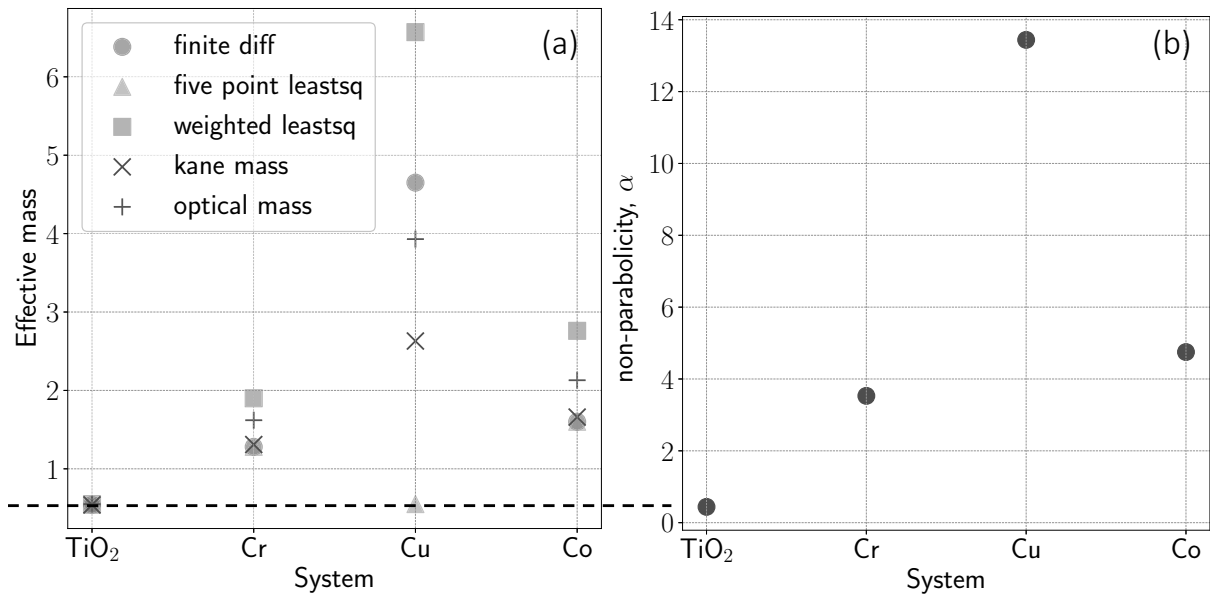


Figure 5.30: (a) Effective masses computed for electrons in the mid-gap states and (b) corresponding  $\alpha$  values

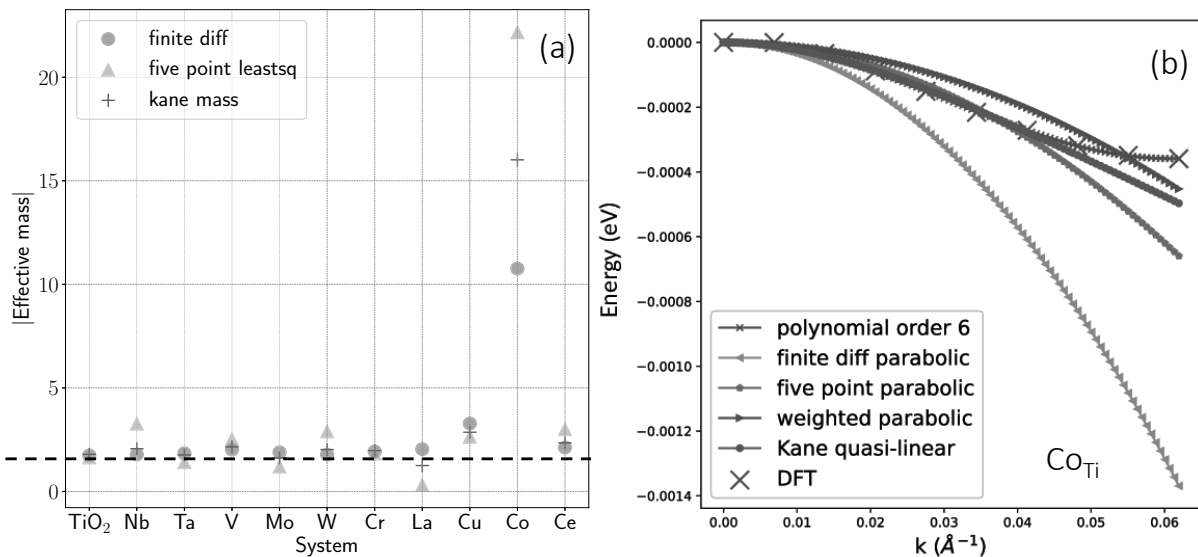


Figure 5.31: (a) Computed effective masses (as multiples of electron rest mass) of holes for various doped systems, (b) Band dispersion fitting at the valence band edge along  $\Gamma-X$  direction for Co-doped anatase

# Chapter 6

## Conclusion

In this work electronic structure calculations for anatase with native defects and doped anatase have been done using *ab initio* DFT. Formation stability and band structure for native defects have been computed. To understand how dopants effect the band curvature of host anatase, a detailed effective mass analysis has been done. To deal with the self-interaction error in DFT, the effective Hubbard  $U$  correction was employed for valence electrons in localized outer  $d$  and  $f$  orbitals. The effective parameter for this correction was determined self-consistently from first-principles using the linear response method [31]. Using a  $U_{eff}$  value of 5.26 eV for Ti, a band gap of 2.72 eV for pristine anatase was obtained. This is still an underestimation with respect to the experimental value, but much better than the values obtained using GGA alone.

Calculations for the native defects showed that O vacancies (for charged states 0, +1) and Ti interstitials (for all the charged states) were associated with localized Ti  $3d$  defect states in the band gap, whereas Ti vacancies and O interstitials formed delocalized O  $2p$  states in the valence band. The gap state was quite close to the conduction band edge in case of  $V_O^{+1}$ . In addition to the localized states, Ti interstitials also formed delocalized states in the conduction band (with Fermi level located inside the conduction band for  $Ti_i$  and  $Ti_i^{+1}$ ). These factors explained the intrinsic conductivity in anatase. The most stable charged states for Ti and O vacancies, Ti interstitials were found to be -4, +2 and +4 respectively, indicating these as quadruple acceptor, double donor and quadruple donor respectively. Moreover, oxygen deficient anatase was predicted here to be intrinsically  $n$ -type. To sum up, native defects have the capability to impart improved conductivity to anatase.

Calculations for doped systems showed that while some dopants like Mo, W, Cr, Cu and Co formed mid-gap states, others like Nb, Ta, V, La and Ce did not form any mid gap states. Among the dopant forming mid-gap states, Mo, Cr, Cu and Co formed multiple mid gap states. Such states could reduce the transparency of the host anatase material, because of the possible electron transitions to mid gap states from the valence band (absorbing light of certain wavelengths in the process). However, in the case of W, a single unoccupied mid gap state was formed, which could reduce the transparency but not as much as in the other dopants forming multiple mid gap states. The Fermi level was positioned near the conduction band edge in case of Nb, Ta and W, which would mean that these doped systems would show improved conductivity. Moreover, Nb and Ta dopants did not form any mid gap states.

In the effective mass analysis for pristine anatase, we were able to reproduce the observed anisotropy in the effective masses of electrons along perpendicular directions. Effective mass for electrons along the  $\Gamma-Z$  direction was found to be almost 10 times higher than that along the  $\Gamma-X$  direction. Dopants increased the effective masses for electrons at the CBM. The increment

in optical effective mass was higher for the dopants Ta, Nb and W than the other dopants. It was also observed that dopants increased the non-parabolicity of bands and a parameter  $\alpha$  was used to quantify this non-parabolicity. Nb-doped system showed a significantly high value of  $\alpha$ , which indicates high non-parabolicity at the conduction band edge for this system. Due to this non-parabolicity, the effective mass values (computed using various definitions) for this system differed significantly from each other. Effective masses calculated for electrons in the mid gap states were found to be quite higher ( $\approx 10$  times more than electrons at CBM) indicating the flat nature of mid gap states. This could mean that the electrons in these states would be highly localized. Among all the dopants considered, Nb, Ta and W doped anatase systems were identified as being better for optoelectronic (TCO) applications. For W-doped anatase, the experimental reports investigating optoelectronic applications are quite rare and hence more experimental investigation could possibly confirm the theoretical predictions from this study.

# Bibliography

- [1] D. S. Sholl and J. A. Steckel, *Density Functional Theory: A Practical Introduction*. Wiley, 2009.
- [2] Y. Luo, A. Benali, L. Shulenburger, J. T. Krogel, O. Heinonen, and P. R. Kent, “Phase stability of TiO<sub>2</sub> polymorphs from diffusion Quantum Monte Carlo,” *New J. Phys.*, vol. 18, no. 11, p. 113049, 2016.
- [3] T. Luttrell, S. Halpegamage, J. Tao, A. Kramer, E. Sutter, and M. Batzill, “Why is anatase a better photocatalyst than rutile?-Model studies on epitaxial TiO<sub>2</sub> films,” *Sci. Rep.*, vol. 4, no. 1, pp. 1–8, 2014.
- [4] J. Zhang, P. Zhou, J. Liu, and J. Yu, “New understanding of the difference of photocatalytic activity among anatase, rutile and brookite TiO<sub>2</sub>,” *Phys. Chem. Chem. Phys.*, vol. 16, no. 38, pp. 20382–20386, 2014.
- [5] T. Hitosugi, N. Yamada, S. Nakao, Y. Hirose, and T. Hasegawa, “Properties of TiO<sub>2</sub>-based transparent conducting oxides,” *Physica status solidi (a)*, vol. 207, no. 7, pp. 1529–1537, 2010.
- [6] T. Hitosugi, A. Ueda, Y. Furubayashi, Y. Hirose, S. Konuma, T. Shimada, and T. Hasegawa, “Fabrication of TiO<sub>2</sub>-Based Transparent Conducting Oxide Films on Glass by Pulsed Laser Deposition,” *Jpn. J. Appl. Phys.*, vol. 46, no. 1L, p. L86, 2007.
- [7] D.-m. Chen, G. Xu, L. Miao, L.-h. Chen, S. Nakao, and P. Jin, “W-doped anatase TiO<sub>2</sub> transparent conductive oxide films: Theory and experiment,” *J. Appl. Phys.*, vol. 107, no. 6, p. 063707, 2010.
- [8] A. Fujishima and K. Honda, “Electrochemical Photolysis of Water at a Semiconductor Electrode,” *Nature*, vol. 238, no. 5358, pp. 37–38, 1972.
- [9] K. Nakata and A. Fujishima, “TiO<sub>2</sub> photocatalysis: Design and applications,” *J. Photochem. Photobiol., C*, vol. 13, no. 3, pp. 169–189, 2012.
- [10] R. A. Afre, N. Sharma, M. Sharon, and M. Sharon, “Transparent Conducting Oxide Films for Various Applications: A Review,” *Rev. Adv. Mater. Sci.*, vol. 53, no. 1, pp. 79–89, 2018.
- [11] S. Ye, A. R. Rathmell, Z. Chen, I. E. Stewart, and B. J. Wiley, “Metal Nanowire Networks: The Next Generation of Transparent Conductors,” *Adv. Mater.*, vol. 26, no. 39, pp. 6670–6687, 2014.
- [12] S. R. Taylor and S. M. McLennan, “The continental crust: Its composition and evolution,” 1985.

- [13] R. Abe, "Recent progress on photocatalytic and photoelectrochemical water splitting under visible light irradiation," *J. Photochem. Photobiol. C: Photochem. Rev.*, vol. 11, no. 4, pp. 179–209, 2010.
- [14] T. Inoue, A. Fujishima, S. Konishi, and K. Honda, "Photoelectrocatalytic reduction of carbon dioxide in aqueous suspensions of semiconductor powders," *Nature*, vol. 277, no. 5698, pp. 637–638, 1979.
- [15] L. Caballero, K. Whitehead, N. Allen, and J. Verran, "Inactivation of *Escherichia coli* on immobilized TiO<sub>2</sub> using fluorescent light," *J. Photochem. Photobiol., A*, vol. 202, no. 2-3, pp. 92–98, 2009.
- [16] H. Tang, K. Prasad, R. Sanjines, P. Schmid, and F. Levy, "Electrical and optical properties of TiO<sub>2</sub> anatase thin films," *J. Appl. Phys.*, vol. 75, no. 4, pp. 2042–2047, 1994.
- [17] Y. Furubayashi, T. Hitosugi, Y. Yamamoto, K. Inaba, G. Kinoda, Y. Hirose, T. Shimada, and T. Hasegawa, "A transparent metal: Nb-doped anatase TiO<sub>2</sub>," *Appl. Phys. Lett.*, vol. 86, no. 25, p. 252101, 2005.
- [18] P. Periyat, B. Naufal, and S. G. Ullattil, "A Review on High Temperature Stable Anatase TiO<sub>2</sub> Photocatalysts," in *Materials Science Forum*, vol. 855, pp. 78–93, Trans Tech Publ, 2016.
- [19] R. Liu, X. Zhou, F. Yang, and Y. Yu, "Combination study of DFT calculation and experiment for photocatalytic properties of S-doped anatase TiO<sub>2</sub>," *Appl. Surf. Sci.*, vol. 319, pp. 50–59, 2014.
- [20] Z. Zhao and Q. Liu, "Mechanism of higher photocatalytic activity of anatase TiO<sub>2</sub> doped with nitrogen under visible-light irradiation from density functional theory calculation," *J. Phys. D: Appl. Phys.*, vol. 41, no. 2, p. 025105, 2007.
- [21] E. Finazzi, C. Di Valentin, G. Pacchioni, and A. Selloni, "Excess electron states in reduced bulk anatase TiO<sub>2</sub>: Comparison of standard GGA, GGA+*U*, and hybrid DFT calculations," *J. Chem. Phys.*, vol. 129, no. 15, p. 154113, 2008.
- [22] S. Na-Phattalung, M. F. Smith, K. Kim, M.-H. Du, S.-H. Wei, S. Zhang, and S. Limpijumnong, "First-principles study of native defects in anatase TiO<sub>2</sub>," *Phys. Rev. B*, vol. 73, no. 12, p. 125205, 2006.
- [23] N. D. Abazović, M. I. Čomor, M. D. Dramićanin, D. J. Jovanović, S. P. Ahrenkiel, and J. M. Nedeljković, "Photoluminescence of Anatase and Rutile TiO<sub>2</sub> Particles," *J. Phys. Chem. B*, vol. 110, no. 50, pp. 25366–25370, 2006.
- [24] T. Berger, M. Sterrer, O. Diwald, E. Knözinger, D. Panayotov, T. L. Thompson, and J. T. Yates, "Light-Induced Charge Separation in Anatase TiO<sub>2</sub> Particles," *J. Phys. Chem. B*, vol. 109, no. 13, pp. 6061–6068, 2005.
- [25] B. J. Morgan and G. W. Watson, "Intrinsic n-type Defect Formation in TiO<sub>2</sub>: A Comparison of Rutile and Anatase from GGA+*U* Calculations," *J. Phys. Chem. C*, vol. 114, no. 5, pp. 2321–2328, 2010.

- [26] J. Osorio-Guillén, S. Lany, and A. Zunger, “Atomic Control of Conductivity Versus Ferromagnetism in Wide-Gap Oxides Via Selective Doping: V, Nb, Ta in Anatase TiO<sub>2</sub>,” *Phys. Rev. Lett.*, vol. 100, no. 3, p. 036601, 2008.
- [27] T. Umebayashi, T. Yamaki, H. Itoh, and K. Asai, “Analysis of electronic structures of 3d transition metal-doped TiO<sub>2</sub> based on band calculations,” *J. Phys. Chem. Solids*, vol. 63, no. 10, pp. 1909–1920, 2002.
- [28] Y. Wang, R. Zhang, J. Li, L. Li, and S. Lin, “First-principles study on transition metal-doped anatase TiO<sub>2</sub>,” *Nanoscale Res. Lett.*, vol. 9, no. 1, pp. 1–8, 2014.
- [29] X. Han, K. Song, L. Lu, Q. Deng, X. Xia, and G. Shao, “Limitation and extrapolation correction of the GGA+*U* formalism: a case study of Nb-doped anatase TiO<sub>2</sub>,” *J. Mater. Chem. C*, vol. 1, no. 23, pp. 3736–3746, 2013.
- [30] W. Chen, P. Yuan, S. Zhang, Q. Sun, E. Liang, and Y. Jia, “Electronic properties of anatase TiO<sub>2</sub> doped by lanthanides: A DFT+*U* study,” *Phys. B: Condens. Matter*, vol. 407, no. 6, pp. 1038–1043, 2012.
- [31] M. Cococcioni and S. de Gironcoli, “Linear response approach to the calculation of the effective interaction parameters in the LDA+*U* method,” *Phys. Rev. B*, vol. 71, p. 035105, 2005.
- [32] T. Hitosugi, H. Kamisaka, K. Yamashita, H. Nogawa, Y. Furubayashi, S. Nakao, N. Yamada, A. Chikamatsu, H. Kumigashira, M. Oshima, *et al.*, “Electronic Band Structure of Transparent Conductor: Nb-Doped Anatase TiO<sub>2</sub>,” *Appl. Phys Express*, vol. 1, no. 11, p. 111203, 2008.
- [33] K. Hongo, N. T. Cuong, and R. Maezono, “The Importance of Electron Correlation on Stacking Interaction of Adenin-Thymine Base-Pair Step in B-DNA: A Quantum Monte Carlo Study,” *J. Chem. Theory Comput.*, vol. 9, no. 2, pp. 1081–1086, 2013.
- [34] K. S. Qin, T. Ichibha, K. Hongo, and R. Maezono, “Inconsistencies in *ab initio* evaluations of non-additive contributions of DNA stacking energies,” *Chem. Phys.*, vol. 529, p. 110554, 2020.
- [35] W. Kohn and L. J. Sham, “Self-Consistent Equations Including Exchange and Correlation Effects,” *Phys. Rev.*, vol. 140, no. 4A, pp. A1133–A1138, 1965.
- [36] F. Bloch, “Über Die Quantenmechanik der Elektronen in Kristallgittern,” *Zeitschrift für physik*, vol. 52, no. 7, pp. 555–600, 1929.
- [37] H. J. Monkhorst and J. D. Pack, “Special points for Brillouin-zone integrations,” *Phys. Rev. B*, vol. 13, p. 5188, 1976.
- [38] D. R. Hamann, M. Schlüter, and C. Chiang, “Norm-conserving pseudopotentials,” *Phys. Rev. Lett.*, vol. 43, pp. 1494–1497, 1979.
- [39] P. E. Blöchl, “Projector augmented-wave method,” *Phys. Rev. B*, vol. 50, p. 17953, 1994.
- [40] G. Kresse and D. Joubert, “From ultrasoft pseudopotentials to the projector augmented-wave method,” *Phys. Rev. B*, vol. 59, p. 1758, 1999.

- [41] J. P. Perdew and A. Zunger, “Self-Consistent Equations Including Exchange and Correlation Effects,” *Phys. Rev. B*, vol. 23, pp. 5048–5079, 1981.
- [42] P. Ziesche, S. Kurth, and J. P. Perdew, “Density functionals from LDA to GGA,” *Comput. Mater. Sci.*, vol. 11, no. 2, pp. 122–127, 1998.
- [43] J. P. Perdew, K. Burke, and M. Ernzerhof, “Generalized Gradient Approximation Made Simple,” *Phys. Rev. Lett.*, vol. 77, p. 3865, 1996.
- [44] K. Burke, J. P. Perdew, and Y. Wang, “Derivation of a Generalized Gradient Approximation: The PW91 Density Functional,” in *Electronic density functional theory*, pp. 81–111, Springer, 1998.
- [45] S. L. Dudarev, G. A. Botton, S. Y. Savrasov, C. J. Humphreys, and A. P. Sutton, “Electron-energy-loss spectra and the structural stability of nickel oxide: An LSDA+ $U$  study,” *Phys. Rev. B*, vol. 57, pp. 1505–1509, 1998.
- [46] M. Lazzeri, C. Attaccalite, L. Wirtz, and F. Mauri, “Impact of the electron-electron correlation on phonon dispersion: Failure of LDA and GGA DFT functionals in graphene and graphite,” *Phys. Rev. B*, vol. 78, p. 081406(R), 2008.
- [47] R. J. Maurer, C. Freysoldt, A. M. Reilly, J. G. Brandenburg, O. T. Hofmann, T. Björkman, S. Lebègue, and A. Tkatchenko, “Advances in Density-Functional Calculations for Materials Modeling,” *Annu. Rev. Mater. Res.*, vol. 49, pp. 1–30, 2019.
- [48] L. Schimka, J. Harl, and G. Kresse, “Improved hybrid functional for solids: The HSEsol functional,” *J. Chem. Phys.*, vol. 134, no. 2, p. 024116, 2011.
- [49] A. D. Becke and M. R. Roussel, “Exchange holes in inhomogeneous systems: A coordinate-space model,” *Phys. Rev. A*, vol. 39, no. 8, p. 3761, 1989.
- [50] A. D. Becke and E. R. Johnson, “A simple effective potential for exchange,” *J. Chem. Phys.*, vol. 124, no. 22, p. 221101, 2006.
- [51] J. Hubbard, “Electron correlations in narrow energy bands,” *Proc. Math. Phys.*, vol. 276, no. 1365, pp. 238–257, 1963.
- [52] V. I. Anisimov, J. Zaanen, and O. K. Andersen, “Band theory and Mott insulators: Hubbard  $U$  instead of Stoner  $I$ ,” *Phys. Rev. B*, vol. 44, pp. 943–954, 1991.
- [53] T. Yanai, G. I. Fann, Z. Gan, and R. J. Harrison, “Multiresolution quantum chemistry in multiwavelet bases: Analytic derivatives for Hartree-Fock and density functional theory,” *J. Chem. Phys.*, vol. 121, p. 2866, 2004.
- [54] L. D. Whalley, “effmass: An effective mass package,” *J. Open Source Softw.*, vol. 3, no. 28, p. 797, 2018.
- [55] N. W. Ashcroft, N. D. Mermin, *et al.*, “Solid state physics,” 1976.
- [56] V. Ariel, “Effective Mass and Energy-Mass Relationship,” *arXiv preprint arXiv:1205.3995*, 2012.
- [57] E. O. Kane, “Band structure of indium antimonide,” *J. Phys. Chem. Solids*, vol. 1, no. 4, pp. 249–261, 1957.

- [58] H. A. Huy, B. Aradi, T. Frauenheim, and P. Deák, “Calculation of carrier-concentration-dependent effective mass in Nb-doped anatase crystals of  $\text{TiO}_2$ ,” *Phys. Rev. B*, vol. 83, no. 15, p. 155201, 2011.
- [59] D. M. Riffe, “Temperature dependence of silicon carrier effective masses with application to femtosecond reflectivity measurements,” *JOSA B*, vol. 19, no. 5, pp. 1092–1100, 2002.
- [60] G. Hautier, A. Miglio, G. Ceder, G.-M. Rignanese, and X. Gonze, “Identification and design principles of low hole effective mass p-type transparent conducting oxides,” *Nat. Commun.*, vol. 4, no. 1, pp. 1–7, 2013.
- [61] P. Giannozzi, S. Baroni, N. Bonini, M. Calandra, R. Car, C. Cavazzoni, D. Ceresoli, G. L. Chiarotti, M. Cococcioni, I. Dabo, A. D. Corso, S. Fabris, G. Fratesi, S. de Gironcoli, R. Gebauer, U. Gerstmann, C. Gougoussis, A. Kokalj, M. Lazzeri, L. Martin-Samos, N. Marzari, F. Mauri, R. Mazzarello, S. Paolini, A. Pasquarello, L. Paulatto, C. Sbraccia, S. Scandolo, G. Sclauzero, A. P. Seitsonen, A. Smogunov, P. Umari, and R. M. Wentzcovitch, “QUANTUM ESPRESSO: a modular and open-source software project for quantum simulations of materials,” *J. Phys. Condens. Matter*, vol. 21, p. 395502, 2009.
- [62] G. Kresse and J. Hafner, “*Ab initio* molecular dynamics for liquid metals,” *Phys. Rev. B*, vol. 47, p. 558, 1993.
- [63] G. Kresse and J. Hafner, “*Ab initio* molecular dynamics simulation of the liquid-metal-amorphous-semiconductor transition in germanium,” *Phys. Rev. B*, vol. 49, p. 14251, 1994.
- [64] G. Kresse and J. Furthmüller, “Efficiency of *ab initio* total energy calculations for metals and semiconductors using a plane-wave basis set,” *Comput. Mater. Sci.*, vol. 6, p. 15, 1996.
- [65] G. Kresse and J. Furthmüller, “Efficient iterative schemes for *ab initio* total-energy calculations using a plane-wave basis set,” *Phys. Rev. B*, vol. 54, p. 11169, 1996.
- [66] M. Yu and D. R. Trinkle, “Accurate and efficient algorithm for Bader charge integration,” *J. Chem. Phys.*, vol. 134, no. 6, p. 064111, 2011.
- [67] G. Henkelman, A. Arnaldsson, and H. Jónsson, “A fast and robust algorithm for Bader decomposition of charge density,” *Comput. Mater. Sci.*, vol. 36, no. 3, pp. 354–360, 2006.
- [68] S. K. Gharaei, M. Abbasnejad, and R. Maezono, “Bandgap reduction of photocatalytic  $\text{TiO}_2$  nanotube by Cu doping,” *Sci. Rep.*, vol. 8, no. 1, pp. 1–10, 2018.
- [69] B. J. Morgan, D. O. Scanlon, and G. W. Watson, “Small polarons in Nb- and Ta-doped rutile and anatase  $\text{TiO}_2$ ,” *J. Mater. Chem.*, vol. 19, no. 29, pp. 5175–5178, 2009.
- [70] F. Labat, P. Baranek, C. Domain, C. Minot, and C. Adamo, “Density functional theory analysis of the structural and electronic properties of  $\text{TiO}_2$  rutile and anatase polytypes: Performances of different exchange-correlation functionals,” *J. Chem. Phys.*, vol. 126, no. 15, p. 154703, 2007.
- [71] M. Mohamad, B. U. Haq, R. Ahmed, A. Shaari, N. Ali, and R. Hussain, “A density functional study of structural, electronic and optical properties of titanium dioxide: Characterization of rutile, anatase and brookite polymorphs,” *Mater. Sci. Semicond. Process.*, vol. 31, pp. 405–414, 2015.



- [72] E. Araujo-Lopez, L. A. Varilla, N. Seriani, and J. A. Montoya, "TiO<sub>2</sub> anatase's bulk and (001) surface, structural and electronic properties: A DFT study on the importance of Hubbard and van der Waals contributions," *Surf. Sci.*, vol. 653, pp. 187–196, 2016.
- [73] E. German, R. Faccio, and A. W. Mombrú, "A DFT+*U* study on structural, electronic, vibrational and thermodynamic properties of TiO<sub>2</sub> polymorphs and hydrogen titanate: tuning the Hubbard '*U*-term'," *J. Phys. Commun.*, vol. 1, no. 5, p. 055006, 2017.
- [74] D. Koch and S. Manzhos, "On the Charge State of Titanium in Titanium Dioxide," *J. Phys. Chem. Lett.*, vol. 8, no. 7, pp. 1593–1598, 2017.
- [75] D. Reyes-Coronado, G. Rodríguez-Gattorno, M. Espinosa-Pesqueira, C. Cab, R. De Coss, and G. Oskam, "Phase-pure TiO<sub>2</sub> nanoparticles: anatase, brookite and rutile," *Nanotechnology*, vol. 19, no. 14, p. 145605, 2008.
- [76] J. K. Burdett, T. Hughbanks, G. J. Miller, J. W. Richardson Jr, and J. V. Smith, "Structural-Electronic Relationships in Inorganic Solids: Powder Neutron Diffraction Studies of the Rutile and Anatase Polymorphs of Titanium Dioxide at 15 and 295 K," *J. Am. Chem. Soc.*, vol. 109, no. 12, pp. 3639–3646, 1987.
- [77] F. Tran and P. Blaha, "Accurate Band Gaps of Semiconductors and Insulators with a Semilocal Exchange-Correlation Potential," *Phys. Rev. Lett.*, vol. 102, no. 22, p. 226401, 2009.
- [78] H. Dietrich, "Tables of Interatomic Distances and Configuration in Molecules and Ions, herausgeg. von AD Mitchell und LC Cross. Special Publication No. 11. Wiss. Herausgeber: LE Sutton. The Chemical Society, London 1958. 1. Aufl., 385 S., geb.£ 2.2. 0," *Angew. Chem.*, vol. 73, no. 14, pp. 511–512, 1961.
- [79] V. Anitha, A. N. Banerjee, and S. W. Joo, "Recent developments in TiO<sub>2</sub> as n- and p-type transparent semiconductors: synthesis, modification, properties, and energy-related applications," *J. Mater. Sci.*, vol. 50, no. 23, pp. 7495–7536, 2015.
- [80] S. Muhammadiyah, E. Nurfani, R. Kurniawan, I. M. Sutjahja, T. Winata, and Y. Darma, "The effect of Ta dopant on the electronic and optical properties of anatase TiO<sub>2</sub>: a first-principles study," *Mater. Res. Express*, vol. 4, no. 2, p. 024002, 2017.
- [81] T. Hitosugi, Y. Furubayashi, A. Ueda, K. Itabashi, K. Inaba, Y. Hirose, G. Kinoda, Y. Yamamoto, T. Shimada, and T. Hasegawa, "Ta-doped Anatase TiO<sub>2</sub> Epitaxial Film as Transparent Conducting Oxide," *Jpn. J. Appl. Phys.*, vol. 44, no. 8L, p. L1063, 2005.
- [82] M. Khan, J. Xu, N. Chen, and W. Cao, "Electronic and optical properties of pure and Mo doped anatase TiO<sub>2</sub> using GGA and GGA+*U* calculations," *Phys. B: Condens. Matter*, vol. 407, no. 17, pp. 3610–3616, 2012.
- [83] R. Zhang, J. Zhao, Y. Yang, Z. Lu, and W. Shi, "Understanding electronic and optical properties of La and Mn co-doped anatase TiO<sub>2</sub>," *Comput. Condens. Matter*, vol. 6, pp. 5–17, 2016.
- [84] H. Kamisaka, T. Hitosugi, T. Suenaga, T. Hasegawa, and K. Yamashita, "Density functional theory based first-principle calculation of Nb-doped anatase TiO<sub>2</sub> and its interactions with oxygen vacancies and interstitial oxygen," *J. Chem. Phys.*, vol. 131, no. 3, p. 034702, 2009.

# Biography

<b>Name</b>	Mr. Abhishek Raghav
<b>Date of Birth</b>	20 July 1996
<b>Educational Attainment</b>	M. Tech in Materials Science & Engineering: Indian Institute of Technology Gandhinagar, Gujarat, India, 2019  B. Tech in Mechanical Engineering: Institute of Engineering and Technology, Alwar, India, 2017
<b>Scholarship</b>	2019-2022: Monbukagakusho (MEXT) Scholarship

## Work Experiences

## Publications

- [1] A. Raghav, K. Utimula, M. Abbasnejad, R. Maezono, and E. Panda “Intrinsic electronic defect states of anatase using density functional theory” *Comput. Mater. Sci.*, vol. 184, p. 109925, 2020
- [2] R. Dahule, A. Raghav, A.T. Hanindriyo, K. Hongo, R. Maezono, and E. Panda, “Surface Study of  $\text{Cu}_2\text{SnS}_3$  Using First-Principles Density Functional Theory” *Adv. Theory Simul.*, vol. r, p. 2000315, 2021
- [3] K. Nakano, A. Raghav and S. Sorella, “Space-warp coordinate transformation for efficient ionic force calculations in quantum Monte Carlo” *J. Chem. Phys.*, vol. 156, p. 034101, 2022
- [4] A. Raghav, K. Hongo, R. Maezono and E. Panda, “Electronic structure and effective mass analysis of doped  $\text{TiO}_2$  (anatase) systems using DFT+ $U$ ” *Comput. Mater. Sci.*, vol. 214, p. 111714, 2022